J. Fluid Mech. (2025), *vol.* 1020, A7, doi:10.1017/jfm.2025.10600

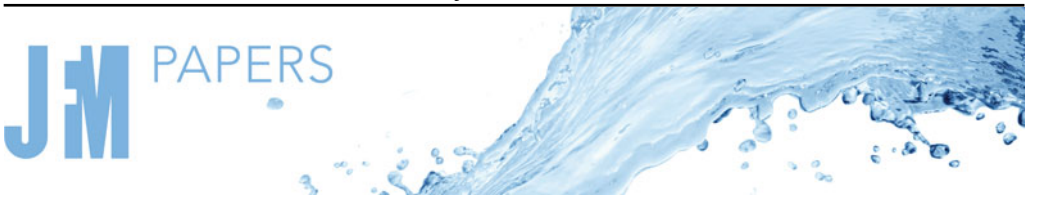

Fall of a group of confined cylinders in a liquid at rest at moderate Reynolds number

Dylan Letessier[1], **Patricia Ern**[1] **and Véronique Roig**[1]

[1]Institut de Mécanique des Fluides de Toulouse (IMFT), Université de Toulouse, CNRS, INPT, Université Toulouse III – Paul Sabatier (UPS), Toulouse, France

Corresponding author: Véronique Roig, roig@imft.fr

(Received 15 February 2025; revised 8 July 2025; accepted 12 August 2025)

Inertial sedimentation of a cloud of cylinders released within a confined fluid-filled cell is experimentally investigated. Various cylinder numbers, N_c, aspect ratios, ξ, solid-to-fluid density ratios, ρ_c/ρ_f, and settling velocities corresponding to moderate Reynolds numbers are examined. The parameters correspond to two distinct path regimes for isolated cylinders: oscillatory trajectories for higher-density cylinders and rectilinear sedimentation for lower-density cylinders. In both cases, we observe the formation of subgroups (termed objects of class N) composed of N cylinders in contact, as well as their recombination due to splitting or merging. Depending on the parameters, specific distributions of class-N objects are found. In addition, beyond the formation of individual objects, large-scale vertical columnar structures emerge, made of densely packed objects and alternating regions of ascending and descending fluid. These structures, driven by complex interactions between local clustering and global flow organisation, which persist throughout the sedimentation process, are highly sensitive to ξ. Despite its inner complex dynamics, the group is observed to sediment as a collective entity, with a constant velocity exceeding that of an isolated cylinder. This velocity may be predicted from multi-scale information. Fluctuating velocities of the objects are further analysed. Different mechanisms for horizontal and vertical components are identified. Horizontal fluctuations are related to intrinsic particle mobility, while vertical fluctuations are attributed to strong wakes and vertical streams. Both fluctuations are mainly influenced by the cylinders' aspect ratio, which also affects the structural and spatial distribution of the objects.

Key words: multiphase and particle-laden flows, particle/fluid flow, plumes/thermals

1. Introduction

In order to accurately reproduce real dispersed flows dynamics, predicting models have to take into account the shape anisotropy of the particles and its influence on their interaction behaviour. In fact, manufactured and natural particles are often far from spherical (Voth & Soldati 2017). For moderate to high Reynolds numbers of the particles especially, geometrical anisotropy modifies at the local scale the interplay between translation and rotation of the particle. The differences in the proper and added inertia contributions resulting from anisotropy introduce complex momentum exchanges with the fluid. In addition, vorticity generation at the body surface strongly depends on the orientation of the body in the flow and can involve different length and velocity scales for the relative motion in translation and rotation depending on the body geometry. For instance, for a single particle simply in free fall in fluid at rest, the shape anisotropy strongly influences the occurrence and properties of the different paths and wakes displayed by the particle (see Ern *et al.* 2012 and, for elongated finite-length cylinders, Toupoint, Ern & Roig 2019; Bouchet & Dušek 2024).

As we are interested here in the mechanisms responsible for the internal structuration of swarms composed of elongated finite-length cylinders, for their fall velocity, size and agitation, we can refer to the literature concerning gravity-induced flows such as during the release of a cloud of particles or in sedimenting swarms. It is also important to analyse specific properties associated with the shape of the particles. The literature is wide when flows with low to high Reynolds numbers Re are considered. However, we present the generic observations that were made regardless of the Reynolds number, because in some cases, shape effects prevail over Re ones. Also, the deviation from Stokes flows in the approximation of Oseen is enlightening for inertial flows at larger Re.

The literature concerning the fall of a spherical cloud of particles considers mainly spherical particles in the Stokes regime, both particle and cloud Reynolds numbers being very low. Indeed, since the work of Nitsche & Batchelor (1997) there have been many theoretical and experimental studies (Machu *et al.* 2001; Ekiel-Jezewska, Metzger & Guazzelli 2006; Metzger *et al.* 2007*b*; Guazzelli & Hinch 2011), with extensions to finite Reynolds numbers in the Oseen's regime (Bosse *et al.* 2005*a*,*b*; Subramanian & Koch 2008; Pignatel, Nicolas & Guazzelli 2011) or questions about the impact of the polydispersion of sizes in Oseen's approximation (Faletra *et al.* 2015) or Stokes' one (Hu *et al.* 2024). The focus has primarily been on the temporal evolution of the global shape of the cloud.

From the works of Subramanian & Koch (2008) and Pignatel *et al.* (2011), the fall of such clouds of particles can be considered to depend mainly on three parameters: the number of particles that are released N, then, δ/R_0, i.e. the inertial length $\delta = a/Re_p$ normalised with the macro-scale length of the cloud R_0 (in place of the low Reynolds number $Re_p = aV_\infty/\nu_f$), and finally, the Reynolds number of the cloud $Re_C = V_0R_0/\nu_f$ (where a and ν_f are respectively the particle size and the kinematic viscosity of the fluid, V_∞ and V_0 are the terminal velocity of the particle and the fall velocity of the group). These parameters allow one to identify three different regimes. The first regime is the Stokes one, when $Re_p << 1$ and $Re_C << 1$, where a destabilisation of a spherical cloud leads to a torus shape that finally breaks in a cascade of toroidal sub-clouds due to leakage of particles at the rear part of the cloud (Nitsche & Batchelor 1997; Machu *et al.* 2001; Metzger *et al.* 2007*b*). Then, when inertia appears, that is, when Oseen's approximation reproduces the local flow around the particles, two other regimes can be distinguished. The first one called the macro-scale inertial regime appears when $Re_C \approx 1$ (Bosse *et al.* 2005*a*,*b*). In this case $\delta > R_0$. Another regime called the micro-scale inertial regime can be observed when $\delta \approx R_0$ or $< R_0$ (Subramanian & Koch 2008; Pignatel *et al.* 2011). In both inertial regimes the clouds appeared to destabilise like in Stokes' regime, showing

a sequence of toroidal deformations and ruptures (Bosse *et al.* 2005*a*; Pignatel *et al.* 2011). But the leading mechanism for this instability is completely different from the one in Stokes' regime: it is governed by an incoming flow at the rear of the cloud. It is generated by the cumulated effects of the Oseen source-sink local velocity field at distances larger than δ (Subramanian & Koch 2008).

The impact of shape anisotropy on flows with settling fibres has also been investigated, as discussed hereafter. Herzhaft *et al.* (1996) and Herzhaft & Guazzelli (1999) observed that in dilute suspensions of settling fibres of elongation ratio between 5 and 32, fibres being in the Stokes regime when isolated, the coupling between the velocity of the centre of mass and the orientation produces rapidly a steady inhomogeneous suspension characterised by the presence of alternating vertical packets and voids of length scale larger than the fibre length. Such destabilisation was also predicted by the numerical simulations of Mackaplow & Shaqfeh (1998) among others. The presence of vertical streams explains that the mean fall velocity is increased up to 1.5 times as compared with the Stokes velocity of an isolated vertical fibre. Intense agitation and large anisotropy of this agitation are observed, where the standard deviation of the vertical velocity fluctuations is up to twice that of horizontal agitation. The probability for a fibre to align in the vertical direction is also quite large. The characteristics associated with large-scale heterogeneities were confirmed and explored in Metzger, Guazzelli & Butler (2005, 2007*a*), Guazzelli & Hinch (2011).

Park *et al.* (2010) also showed that during the release of dilute or semi-dilute finite clouds of non-inertial fibres, a qualitatively similar sequence of destabilisation occurs as compared with clouds of non-inertial spheres. However, the anisotropy of fibres plays an important role. Indeed, the coupling between the self-induced motion and the fluctuations of the flow generates a breakup process developing faster than for spheres.

There is less literature on releases of blobs of inertial particles, and it is limited to spherical particles. They have been primarily studied – typically with Reynolds numbers in the range 50–300 – for applications in hydraulics such as sediment discharge in lakes and oceans concerning monodispersed distributions of particle sizes (Buhler & Papantoniou 1991; Noh & Fernando 1993; Buhler & Papantoniou 2001; Moghadaripour, Azimi & Elyasi 2017) or polydispersed ones (Lai *et al.* 2016).

During the fall of an initially spherical cloud, three distinct phases have been identified by several authors (i.e. Buhler & Papantoniou 1991; Noh & Fernando 1993; Buhler & Papantoniou 2001; Bush, Thurber & Blanchette 2003; Lai *et al.* 2013; Zhao *et al.* 2014; Kriaa *et al.* 2022):

(i) An initial short balistic acceleration of the particles that stay grouped as a solid sphere;
(ii) A self-similar regime where an internal vortex circulation develops and where internal turbulent agitation causes entrainment of ambient fluid in the cloud, similarly to single-phase thermal blobs;
(iii) A final particle-settling regime (or dispersive regime) organised as a bowl-shaped swarm of particles, which settle and propagate far from the decaying turbulence left downstream in the liquid.

In the self-similar thermal regime the velocities of the particles and of the liquid are quite similar, while in the particle-settling regime the velocity of the fluid inside the group of particles is negligible. During the self-similar regime the extent of the fluid–particle mixture increases due to external fluid entrainment. Thus, even if there is no significant

leakage of particles, the mixture becomes more and more diluted as it propagates far from the source and its velocity also decreases. It was proven by Kriaa *et al.* (2022) that these particulate thermals entrain more fluid than a single-phase thermal and that optimal entrainment exists for a Rouse number, comparing the terminal velocity of a particle to the buoyancy-induced liquid velocity, which is around 0.3. In the final particle-settling regime the group velocity is constant, regardless of cloud buoyancy, and is more often observed to be of the order of magnitude of, but higher than, the terminal velocity of the particles (Noh & Fernando 1993; Bush *et al.* 2003; Lai *et al.* 2013; Kriaa *et al.* 2022). Bush *et al.* (2003) also highlighted that the width of the swarm stays nearly constant as the entrainment rate is very low (Lai *et al.* 2013; Kriaa *et al.* 2022).

The existence of these three successive regimes and the conditions for transitions between them have been questioned in the literature. The problem is often framed as involving a single control parameter, such as the Rouse number Ro. Although there are several definitions for this parameter, the underlying idea is that the dynamics depend on the ratio between the terminal velocity of a particle V_∞ and a buoyancy-induced velocity in the liquid most often defined at the injection location U_{f0}, $Ro = (V_\infty/U_{f0})$ (Kriaa *et al.* 2022). Throughout the flow, the local buoyancy-induced velocity $U_f(z)$ decreases with the distance z to the injection due to dilution (Morton, Taylor & Turner 1956). The location z_{trans} of the transition between thermal and particle-settling regimes is predicted to occur when $V_\infty > U_f(z_{trans})$ (Kriaa *et al.* 2022). Noh & Fernando (1993) nevertheless argued that not only this condition, but also another one must be verified. They argued that, in the thermal self-similar regime, to ensure that the fluid is entrained by the particles, it is necessary, moreover, that momentum from the particles be really transmitted to the fluid. This requires that the length scale characteristic of the transport of momentum at local scale, δ, be greater than the mean distance between two particles, d_{12}. In their Oseen's conditions, where $\delta = \nu_f / V_\infty$, this leads to a transition length dependency not only on global buoyant effects but also on the Reynolds number Re_p of the particles. Bush *et al.* (2003) also found a sensitivity of the location of this transition, z_{trans}, to Re_p. In Kriaa *et al.* (2022), z_{trans} evolves only with Ro^{-1}, but, as the authors pointed out, the Rouse number was varied by varying the particle size so that the dependency on Re_p could not be analysed. Finally, for sufficiently large values of Rouse number, Zhao *et al.* (2014) observed the destabilisation of blobs of inertial particles consisting of multiple vertical clumps at the front of the blob.

Other studies on the settling of initially uniform swarms of spherical or ellipsoidal particles at large Reynolds numbers have identified several mechanisms that can lead to clustering at large scale, or that participate in inhibiting it (Kajishima 2004; Uhlmann & Doychev 2014; Zaidi, Tsuji & Tanaka 2014; Fornari *et al.* 2016, 2018; Huisman *et al.* 2016; Seyed-Ahmadi & Wachs 2021; Moriche *et al.* 2023). All these numerical or experimental investigations explored the effect on clustering and falling velocity due to the shape of the particles, their Galileo number, Ga, or to the solid volume fraction, α, for moderate density ratios. They clearly proved that clustering increases fall velocity.

Various studies for spheres or particles with different shapes have shown that the solid volume fraction has to be limited to allow efficient clustering (Zaidi *et al.* 2014; Fornari, Ardekani & Brandt 2018; Seyed-Ahmadi & Wachs 2021). Then, at larger values, the fall velocity decreases compared with the terminal velocity related to the hindrance effect.

In the numerical simulations of Uhlmann & Doychev (2014) and in the experiments of Huisman *et al.* (2016) devoted to dilute swarms of spheres, the authors showed that clustering occurs only for Galileo numbers greater than 155 when a change occurs in the wake and fall regime of an isolated sphere. For lower Galileo values, a sphere is known

to fall steadily in the vertical direction, whereas for higher values of Ga, a sphere falls steadily but in an oblique direction (Uhlmann & Dušek 2014). The transition to oblique path is expected to increase the frequency of particle–particle encounters in a swarm and thereby facilitate cluster formation. For spheres, the mechanism for clustering is thus the wake-induced local perturbation around the particle. From the simulations of Kajishima (2004) where spheres were or were not allowed to rotate, another active mechanism was shown to be able to inhibit clustering formation: indeed, the rotation of particles and the associated lift force make particles easily escape from clusters so that rotating particles may limit cluster formation. This is the mechanism identified by Seyed-Ahmadi & Wachs (2021) to explain that dilute swarms of cubes keep far more homogeneous at a Galileo number equal to 160 compared with swarms of spheres.

In their numerical simulations of dilute sedimentations of oblate spheroids of elongation ratio equal to three and Galileo number equal to 60 corresponding to a stable fall for an isolated particle, Fornari *et al.* (2018) observed the presence of vertical columnar structures. They thus pointed out that a different mechanism takes place to explain clustering. It is the long-life piling-up process during drafting–kissing–tumbling events that create the columns. In fact, the particles were stacked and did not tumble. For a Galileo number equal to 140 in the dilute regime, the clustering was even stronger. Moriche *et al.* (2023) simulated oblate particles with an elongation ratio of 1.5 and a density ratio equal to 1.5. They studied two cases with Galileo numbers equal to 111 and 152 for which the isolated particle motion is, respectively, steady rectilinear and steady oblique. They observed strong clustering in both cases, demonstrating that the path regime of the isolated particle does not control the appearance of clusters for such oblate spheroids. With an analysis of pair interactions for spheres and spheroids, either free to rotate or not, they showed several important points. Spheres free to rotate generate less clustering than non-rotating ones because they have a longer drafting time and separate very rapidly after collision. Oblate spheroids, not allowed or allowed to rotate, pass, respectively, a long period in contact or stay near each other colliding several times. They can thus both easily build clusters. This specific pair interaction of oblate particles is a shape-induced clustering mechanism more than a wake regime one. It governs the piling-up process identified by Fornari *et al.* (2018).

To address the question of the impact of strong anisotropy on interacting particles in relative motion, the present experimental study investigates the free fall of a group of moderate- to high-Reynolds-number cylinders released in water at rest and confined in a planar vertical thin-gap cell of width w. The cylinders have a finite length L and a diameter d. While the elongation ratio $\xi = L/d$ is varied in the various runs, the diameter-to-width ratio d/w is kept constant and equal to 0.8, which ensures that the motion of the cylinders consists of a translation in the plane and a rotation about the direction perpendicular to the cell plane. In fact, Semin *et al.* (2012) and Gianorio *et al.* (2014) reported that, at least for isolated cylinders, for this value of the ratio d/w, the cylinder motion is limited to such components. This confinement, of course, implies that the hydrodynamics is constrained and different from that observed in unconfined flows. However, a recent study on the free fall of isolated cylinders showed that, regardless of the action of confinement, inertial cylinders show behaviours common to confined and unconfined configurations (Letessier, Roig & Ern 2025). As examples, fluttering motions can be observed; the frequency of oscillation of heavy cylinders scales similarly; generic models for the hydrodynamical loads allow one to reproduce the complex kinematics where the coupling between translation and rotation oscillating components is essential. Also, during the release of a swarm of cylinders in such confined geometry, even if three-dimensional liquid turbulent agitation cannot develop freely, random motions induced in

the liquid by the interacting wakes are expected to act on the group of cylinders. If we further refer to our knowledge on the agitation generated in a confined bubble swarm studied by Bouche *et al.* (2014) and to the three-dimensional characterisation of the flow induced by a confined isolated bubble (Pavlov *et al.* 2021), most of the kinetic energy of the agitation generated in the liquid appears in motions mainly parallel to the walls (Pavlov *et al.* 2021), and a continuous spectrum of this kinetic energy is built in between the Eulerian integral length scale identified as the length of the average bubble wakes and the diameter of the bubbles (Bouche *et al.* 2014). Therefore, it can be expected that, in a confined group of cylinders settling in a liquid otherwise at rest, the agitation of the underlying fluid develops a continuous spectrum of length scales for the in-plane motions in between L and the size R of the released group.

The present study explores several generic questions: How does the cloud structure itself at large scale after release? What is its fall velocity? What is its internal spatial organisation and the agitation of the cylinders? By varying different control parameters, we present some scaling laws that may, at the very least, inspire the search for scaling laws in unconfined swarms.

The paper is organised as follows. Section 2 describes the flow configuration and the experimental methods. In § 3 the collective motion of the group, that is its mean velocity, its global shape and size, is discussed, while § 4 reports a description of the spatio-temporal organisation of the cylinders inside the group. Finally, the statistics of the velocities of the objects present in the group are discussed in § 5. A model requiring multi-scale informations is presented for the fall velocity of the group, and scaling laws for the agitation are proposed. Throughout the reported results, the discussion highlights the contrasted anisotropy properties of the characteristic structures and of their velocities observed at various scales, which mainly depend on the elongation ratio of the cylinders.

2. Experimental set-up

2.1. *Experimental conditions*

The fall of a group of cylinders in a thin vertical cell filled with quiescent fluid is investigated. The dimensions of the cell are $h = 80$ cm in height, $l = 40$ cm in width and $w = 1$ mm in thickness (Letessier *et al.* 2025). The diameter of the cylinders is constant and equal to $d = 0.8$ mm, which is comparable to the gap size w. In contrast, the dimensions of the cell, l and h, are large relative to the length L of the cylinders. The release of the group into the thin gap is operated with a trapdoor system consisting of two needles inserted in the cell and held by magnets. The tips of the needles are in contact at the bottom of the pile of cylinders. The cylinders, initially stacked on the needles, begin to fall once the magnets positioned outside the cell are manually removed. A diagram of the set-up and of this system as well as images at different instants are provided in figure 1. The results presented in this paper focus on the analysis of images obtained within the area marked in green on the diagram, located between 20 cm and 40 cm below the release point and within a window 20 cm wide. As will be shown later, this position is sufficiently far from injection to investigate the dynamics of the group in a permanent regime. A Dimax PCO Imaging camera with a resolution of 2016 × 2016 pixels and an acquisition rate of 250 images per second, equipped with a Nikkon AF Micro Nikkor 200 mm lens, was used to record the motions of the cylinders. Each pixel in the image corresponds to a physical width of 0.11 mm, defining the resolution. A backlight LED panel was positioned at the back of the set-up to increase contrast in the images. An identical second camera was used to investigate and characterise the release conditions as illustrated in figure 1(*b*).

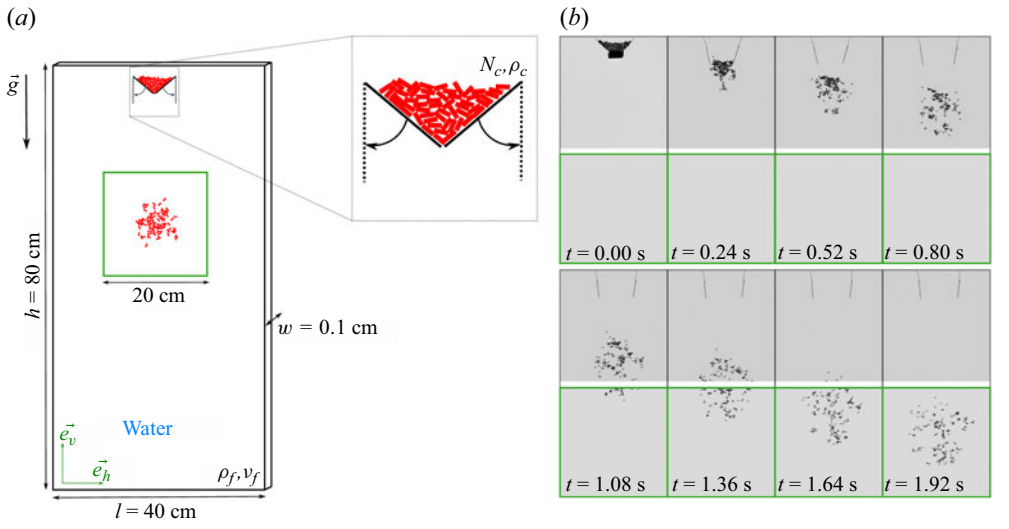

Figure 1. (*a*) Experimental set-up showing cylinders before release and after release in the region of observation (in the zoom-in view, needles are plotted in black and the arrows indicate their motion at the time of release, the pile of cylinders is plotted in red). (*b*) Images from both cameras at eight different times for a release of $N_c = 200$ aluminium cylinders with an aspect ratio $\xi = 5$. In both (*a*) and (*b*) the green area corresponds to the region used for the investigation.

Cylinders with elongation ratios $\xi = (L/d) \in \{3, 5, 10\}$ are considered, made of different materials (density ρ_c) and released in water (density ρ_f, kinematic viscosity ν_f), corresponding to body-to-fluid density ratios $(\rho_c/\rho_f) \in \{1.4, 2.7\}$ and Archimedes numbers $Ar = \sqrt{(\rho_c - \rho_f/\rho_f) g d_{3D}}(d_{3D}/\nu_f) \in \{106, 122, 193, 249, 352\}$, where g is the gravitational acceleration and $d_{3D} = ((3/2)d^2 L)^{(1/3)}$ the diameter of the sphere having the same volume as the cylinder. The density ratios correspond to polyacetal plastic (POMC) and aluminium, respectively. The number of cylinders released in the group, N_c, is varied: $N_c \in \{50, 60, 100, 200, 333\}$. The number N_c is calculated from a global measurement of the mass of the pile of cylinders using a mass balance with a precision of ± 1 mg. The precision of the mass balance and the mass of each type of cylinder allows us to be confident in the number N_c with an error of less than 1 cylinder. Table 1 summarises the different experiments. As reported in this table, for each experimental condition (ρ_c/ρ_f, Ar, ξ, N_c), runs have been repeated – up to 45 times – to obtain statistically converged measurements. Cutting precisely cylinders with elongation ratios lower than 3 is difficult, so to complement the range of elongation ratios considered, we also report some experiments with glass spheres of average diameter $d = 0.8$ mm. Their density is close to that of aluminium. The present analysis mainly focuses on the fall of the groups of cylinders, but when relevant, comments will also be provided for experiments with spheres.

As shown in figure 1, a second camera was used to quantify and check injection conditions. The groups are released from an initial triangular pile built by manual loading. At a given N_c, the initial distribution of cylinders adopts a reproducible nearly triangular shape due to the conical arrangement of the needles as drawn in figure 1. It was not possible to control the initial orientation of the cylinders within each group, but the packing fraction of the different piles before release is reproducible (table 1). The time interval between the first and last cylinders that crossed the vertical position of the needle ends was found to be quite reproducible and approximately equal to 0.5 s. At release, the group that forms is rapidly detached from the injection system and evolves as a whole, but a random

Material	ρ_c/ρ_f	ξ	A_r	N_c	Mass (mg)	No. of runs	α_{c0}	Symbols
Glass spheres	2.5	1	106	400	268	5	0.9 ± 0.05	▲
				800	536	6		■
				1300	871	4		●
Aluminium cylinders	2.7	3	193	100	326	15	0.70 ± 0.02	▲
				200	651	15	0.80 ± 0.04	■
				333	1086	15	0.75 ± 0.07	●
		5	249	60	326	15	0.75 ± 0.05	▲
				100	543	15	0.70 ± 0.08	■
				200	1086	45	0.75 ± 0.06	●
		10	352	50	543	15	0.65 ± 0.04	▲
				100	1086	15	0.60 ± 0.04	■
POM C cylinders	1.4	5	122	100	280	8	0.70 ± 0.1	▲ or △

Table 1. Summary of the cases studied for the fall of groups of cylinders. The initial solid surface fraction prior to release is denoted α_{c0}. Cases with $\xi = 1$ correspond to releases of groups of glass spheres. Matching colours in the N_c column indicate cases with an equal total mass of injected cylinders. The symbols used throughout the paper to represent each case are introduced here. For a given material and aspect ratio, the marker shape indicates the number of cylinders N_c: triangle (lowest N_c), square (intermediate N_c) and circle (highest N_c). Blue markers represent aluminium cylinders and the colour shading encodes the aspect ratio (light to dark blue: $\xi = 3, 5, 10$). Red markers denote glass spheres. Green markers correspond to POMC cylinders.

ρ_c/ρ_f	ξ	Ar	Path	f_θ (s^{-1})	$\overline{u}_\infty$ ($m\,s^{-1}$)	$\sqrt{\overline{u'^2_{v\infty}}}$ ($m\,s^{-1}$)	$\sqrt{\overline{u'^2_{v\infty}}}$ ($m\,s^{-1}$)
2.5	1	106	Rectilinear	—	0.100	0	0
	3	193		7.7	0.093	0.022	0.007
2.7	5	249	Fluttering	5.4	0.085	0.050	0.019
	10	352		3.4	0.070	0.059	0.019
1.4	5	122	Rectilinear	—	0.030	0	0

Table 2. Data related to the isolated cylinder in free fall within the same confined cell (see Letessier *et al.* 2025).

destructuring of the group is then rapidly observed. This led us to analyse the motion statistics from a large number of similar releases. The motions were also recorded in a region of interest sufficiently distant from the inlet to filter out the dependence on the injection conditions.

When isolated cylinders with similar density or elongation ratios are dropped under the same conditions in water at rest, they all exhibit oscillatory trajectories known as fluttering, except for plastic cylinders (POMC), which follow a rectilinear path. Their associated frequency of oscillation, f_θ, mean vertical velocity, $\overline{u}_\infty$, and standard deviations of the horizontal and vertical velocity fluctuations, $\sqrt{\overline{u'^2_{h\infty}}}$ and $\sqrt{\overline{u'^2_{v\infty}}}$, are reported in table 2, as they will be used in the analysis.

2.2. *Object tracking methods*

After conventional image processing, specifically inverting the image, subtracting the background and binarising the images, we used MATLAB's 'regionprops' function to

label all connected pixels in each image. Therefore, in this study the tracking and information gathering concern objects composed of potentially several cylinders in contact. In our images, the transmitted light intensity is too low when two cylinders make contact, hindering effective segmentation. Although single cylinders moving far from the others can be tracked, it is not possible to track each cylinder in objects involving more than two cylinders. Once labelled, these objects need to be tracked over time, prompting the development of a specific and adapted particle tracking velocimetry (PTV) algorithm. Given the high temporal resolution, resulting in only small displacements between consecutive images, this algorithm associates objects frame to frame by finding the closest centre of mass and the most overlapping bounding box. Knowing the number of pixels composing a single cylinder allows the determination of the number of cylinders involved in each object. By maintaining continuity in cylinder count across frames, we can measure the velocity of the centre of mass of the object. Objects are considered to 'die' when the number of cylinders in contact changes due to fusion with another object or self-dissociation, and 'birth' occurs when new objects emerge as others die. In the following, we classify the objects according to the number of cylinders in contact. This number defines the class of the object.

It is important to note that, as in the case of isolated cylinders, observation indicates that the revolution axes of the cylinders remain parallel to the cell and that there is no contact of the surfaces of the cylinders with the walls. In fact, visual observations and post-processing of the velocities show no discontinuity, no stop in the motions and no alteration of the length of the cylinders seen by the camera that could indicate an inclination inside the gap towards the walls.

3. Description of the collective motion: mean velocity, shape and size of the group

In the area of observation, sufficiently far from the injection, the group moves in a regime for which the effect of initial conditions has vanished. The group of cylinders evolves very slowly at large scale as it moves vertically. Its overall extent and the large-scale heterogeneities present in it do not change significantly during the time of observation (around 2 s). Our measurements indicate that the group falls with a constant vertical velocity. However, intense internal agitation is observed in the group. It consists of random motions of the objects that lead to rapid and frequent reconfigurations through breakups and fusions. When observed in the frame moving with the group, these motions present stationary statistics, which will be discussed in §§ 4 and 5. We now investigate how the vertical velocity of the group, its shape and its global extent evolve as a function of the aspect ratio ξ, density ratio ρ_c/ρ_f, Archimedes number Ar and the number of cylinders N_c that are considered. For this purpose, the mean values of the measured quantities have been obtained by averaging from all release experiments for given (ξ, ρ_c/ρ_f, Ar, N_c) conditions (see table 1).

3.1. *The velocity of the falling group*

Figure 2 presents the mean vertical velocity of each group, u_G, as a function of ξ on the left, as well as this velocity normalised with the mean vertical velocity of the isolated body, $\overline{u}_\infty$, on the right. The velocity u_G is the velocity of the centre of mass of the group. It is related to the velocities of the objects weighted by their classes. There are negligible run-to-run variations of the mean velocity. They are of the order of 0.5 mm s^{-1}.

It can be observed in figure 2(a) that, for a given density, mean velocities appear to depend mainly on the aspect ratio of the released objects and, to a lesser extent, on the

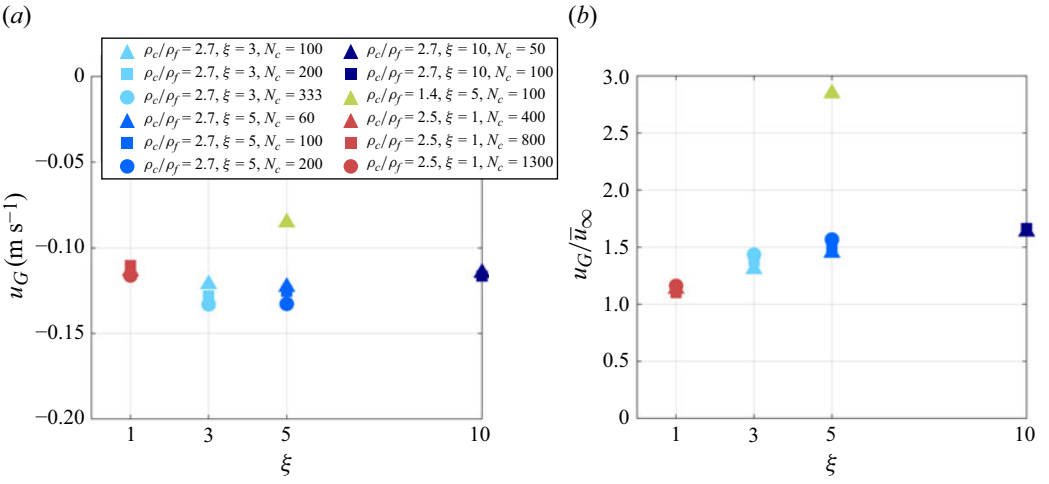

Figure 2. (*a*) Mean vertical velocity u_G as a function of the aspect ratio ξ. (*b*) Mean vertical velocity normalised by the mean vertical velocity of the isolated body $\overline{u}_\infty$ as a function of the aspect ratio. Blue markers are used for aluminium cylinders with $\rho_c/\rho_f = 2.7$, with the intensity of the blue increasing with the elongation ratio; $\xi = 3$: ▲ $N_c = 100$, ■ $N_c = 200$, ● $N_c = 333$; $\xi = 5$: ▲ $N_c = 60$, ■ $N_c = 100$, ● $N_c = 200$; $\xi = 10$: ▲ $N_c = 50$, ■ $N_c = 100$. Red markers are used for glass spheres with $\rho_c/\rho_f = 2.5$ and aspect ratio $\xi_s = 1$: ▲ $N_c = 400$, ■ $N_c = 800$, ● $N_c = 1300$. Green markers are used for POMC cylinders with $\rho_c/\rho_f = 1.4$ and $\xi = 5$: ▲ $N_c = 100$.

number of objects released N_c. For groups of cylinders with a given aspect ratio, an increase in the number of released objects systematically results in a slightly faster descent of the group. A strong effect of the density ratio is also observed: as expected, at $\xi = 5$, groups containing less dense cylinders ($\rho_c/\rho_f = 1.4$) fall more slowly than the aluminium ones with a higher density. The effect of N_c is less sensitive for spheres ($\xi_s = 1$).

Regarding the aspect ratio effect, it was previously observed that, for isolated cylinders in confined cells, at given Ar and ρ_c/ρ_f, shorter cylinders fell more rapidly than longer ones in fluttering regimes (see table 2, and Letessier *et al.* 2025). In the case of groups, this trend is not maintained. This is of course due to the presence of group-induced liquid agitation and to the fact that cylinders may not fall separately, but regroup in objects of complex shape, which will be analysed later on. In addition, the oscillations in velocity and orientation of the single cylinders present in the group are strongly modified relative to the fluttering regime by group-induced liquid agitation. If we compare the fall velocity of the group for a given injected mass, e.g. cases associated with circles or square symbols for aluminium cylinders with the same value of the product $N_c\xi = 1000$, u_G is unchanged for $\xi = 3$ and 5, but clearly different for $\xi = 10$. This indicates that the injected mass is not the unique parameter determining the mean velocity of the group.

On the other hand, in figure 2(*b*), which compares the velocity of the group with that of the isolated body (sphere or cylinder), it can be seen that all groups fall more rapidly than the isolated body. The normalisation does not suppress the dependences on the aspect ratio ξ and on the density ratio. For the spheres, it is observed that the groups fall very slightly faster than the isolated sphere, which falls at $u_\infty = 10\ \mathrm{cm\,s^{-1}}$, a value consistent with the observations made by Lee, Ramos & Swinney (2007) during the sedimentation of spheres in a Hele–Shaw cell. For aluminium cylinders with $\xi \geq 3$, $u_G/\overline{u}_\infty$ increases when the aspect ratio increases. The amplification of the fall velocity reaches 1.66 at $\xi = 10$. Regarding POMC plastic cylinders, the mean velocity achieved by the group is almost

three times that of the isolated cylinder. This significant difference is attributed to the fact that plastic cylinders, due to their low density, are more sensitive to preferential descending entrainment generated by the wakes of surrounding falling objects. The behaviour of the group velocity in the present experiments is similar to that in the final particle-settling regime observed after the release of unconfined clouds of spherical particles at high *Re*: the group velocity approaches the terminal velocity but always keeps larger than it (Buhler & Papantoniou 1991, 2001; Noh & Fernando 1993; Kriaa *et al.* 2022).

3.2. *The mean shape and mean size of the group*

In figure 3 the local solid surface fraction, $\tilde{\alpha}$, obtained by averaging data for all runs, is represented for each set of parameters investigated. The aspect ratio ξ of the cylinders appears to have an important impact on the organisation of the group at the macro scale. As the particles become longer, for all N_c values, the cloud elongates in the vertical direction. The average shape of a group is characterised by the equivalent ellipse associated with the spatial distribution of all the points where $\tilde{\alpha}$ is higher than 1 %. Below this threshold, the solid surface fraction is considered too low to be part of the cloud. The equivalent ellipses are plotted in magenta dashed lines over the distribution of $\tilde{\alpha}$ around their centre (which differs from the centre of mass). For spheres, the average shape of the group is an ellipse having its major axis aligned with the horizontal direction. We define an oriented eccentricity χ as the ratio of the semi-axis in the vertical direction with the semi-axis in the horizontal one. Its values are reported in figure 4. For $N_c = 1300$, the oriented eccentricity is equal to 0.82. The shape and orientation of the ellipse is quite similar for the group of short aluminium cylinders with $\xi = 3$, which have a similar density ratio. Then, for $\xi = 5$, the group shows an average circular shape in the cell plane. And finally, for $\xi = 10$, $N_c = 100$, the ellipse is much more elongated in the vertical direction (oriented eccentricity χ equal to 1.53). This important vertical elongation is observed similarly in groups composed of lighter cylinders with $\xi = 5$ made of POMC plastic. Another characteristic distinguishes the behaviours of the groups of spheres ($\xi = 1$) and cylinders. For the cylinders, higher concentrations at the centre and a gradual decrease toward the edges are observed, whereas the groups of spheres exhibit a rear over-concentration. They are also characterised by a flat rear edge. In contrast to the groups of cylinders, where a cylinder located at the rear eventually no longer experiences the hydrodynamic effects of the group, slows its fall and, thus, participates to a 'leakage' from the group, whereas spheres appear to have more difficulty escaping from the group. The spheres that fall behind the group always tend to rejoin the group. The difference in this possibility of leakage between cylinders and spheres is in agreement with two others observations that can explain it:

(i) The group of spheres falls with less internal large-scale heterogeneities than the groups of cylinders as discussed in § 4.1, and
(ii) The group of spheres falls at a speed very close to that of an isolated sphere, while in groups of cylinders u_G is more enhanced. On the one hand, the larger difference between u_G and $\overline{u}_\infty$ favours the escape of single cylinders from the group. On the other hand, the size and possibility of reorientation of the cylinders make them less sensitive to passive advection by the fluid currents generated by the group, compared with the spheres.

To define a group's size from our measurements, we introduce the radius R of a disk that has the same area as the region where $\tilde{\alpha}$ is higher than 1 %. In figure 3, circles with this radius are shown by a red dashed line around the centre of the latter area. These

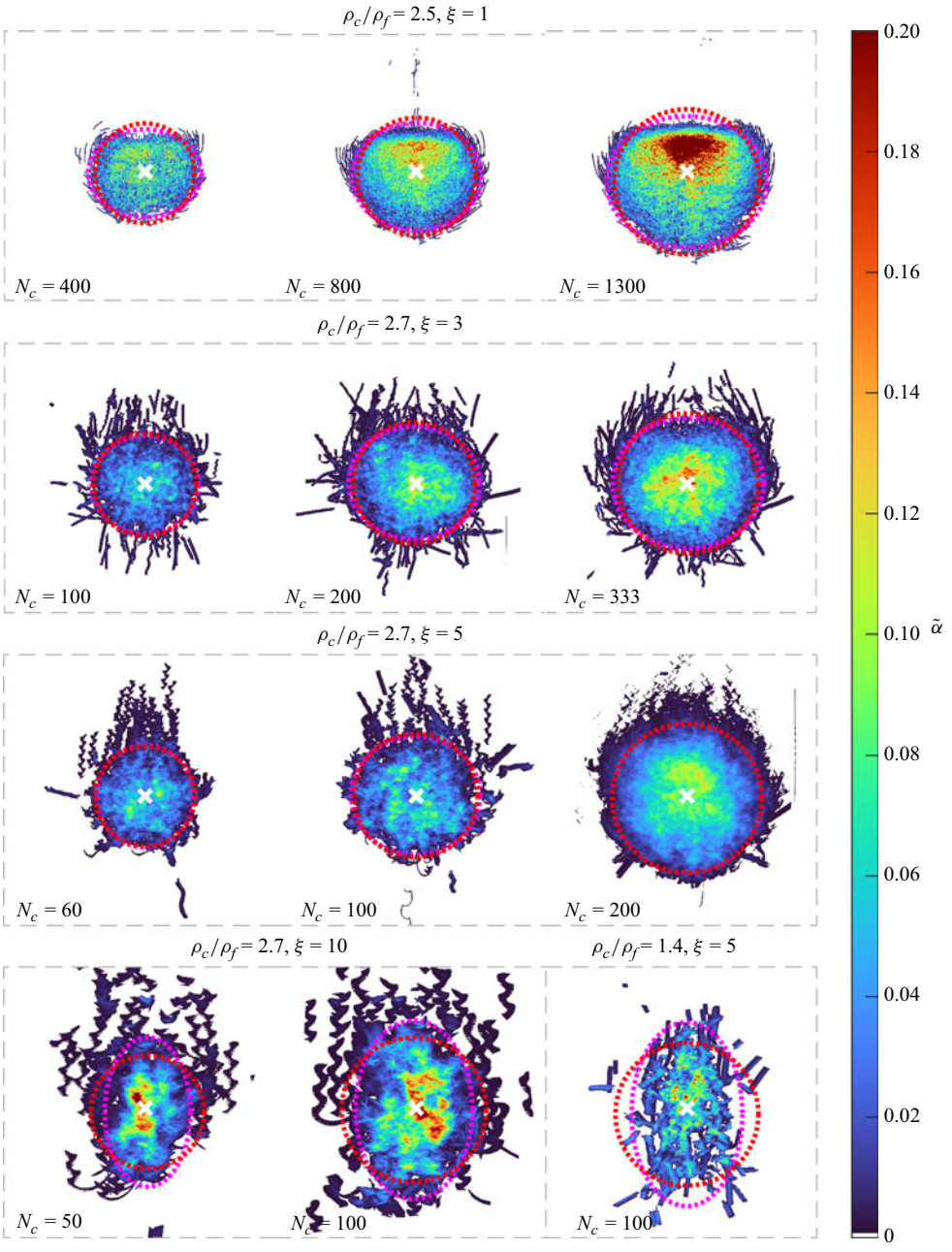

Figure 3. Solid surface fraction $\tilde{\alpha}$ for each injection condition. Magenta dashed lines represent the equivalent ellipse associated with the spatial distribution of all the points where $\tilde{\alpha} > 1$ %. Red dashed lines represent the circle limiting a disk of the same area as the surface where $\tilde{\alpha} > 1$ %. The white cross is the centre of the region where $\tilde{\alpha} > 1$ %.

circles match the mean sizes of the groups, indicating that R satisfactorily represents an overall size of the group. Figure 4(a) illustrates the variation in the radius of the group as a function of the aspect ratio of the particles, using distinct symbols to represent different numbers of released particles. It is observed that the measured radius is weakly influenced

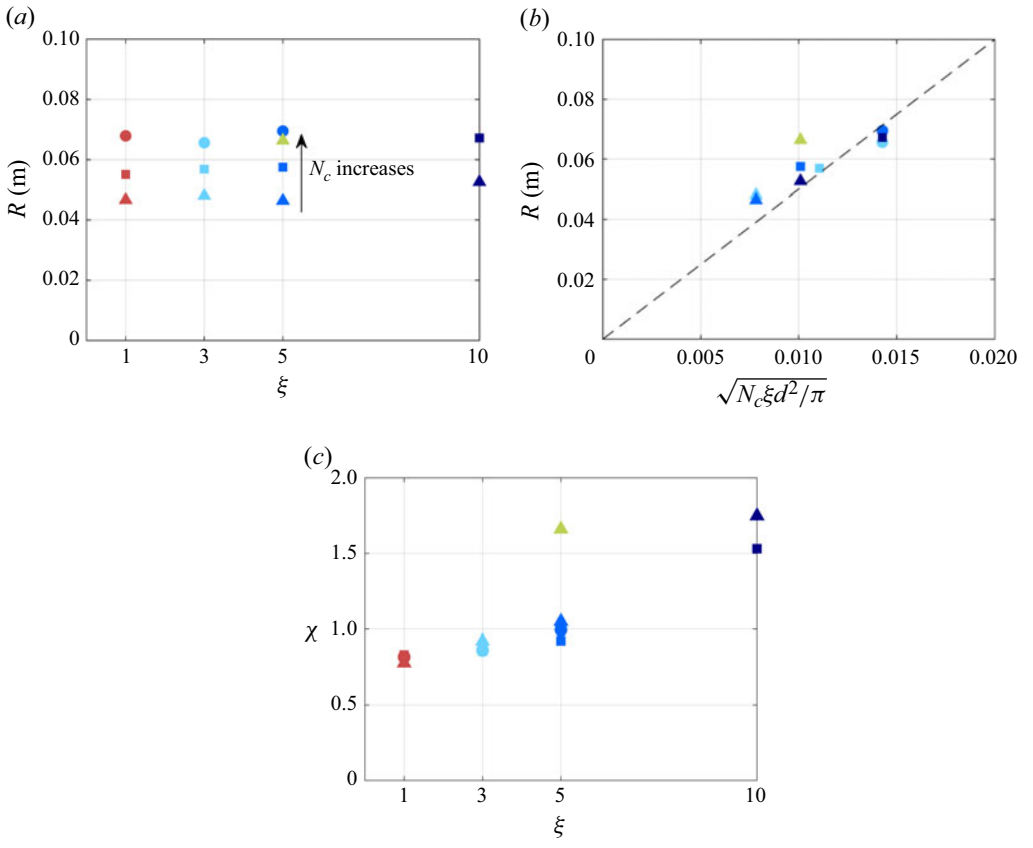

Figure 4. Radius of the falling group R as a function of (a) the aspect ratio ξ and (b) the radius of the disk having the same area as N_c cylinders. The black dashed line represents $R = 5\sqrt{N_c \xi d^2/\pi}$. ($c$) 'Oriented' eccentricity χ of the ellipse equivalent to the group. Same legend as in figure 2.

by the aspect ratio ξ, but mainly depends on the number of cylinders released. Indeed, as the number of particles increases, so does the group's radius. Additionally, for groups composed of cylinders, the measured radius can be compared with the equivalent radius corresponding to their cumulative area, given by $\sqrt{N_c \xi d^2/\pi}$ for maximum compaction (figure 4b). The measured radius is approximately five times larger than this reference radius. This relationship is observed despite slight variations in the initial packing fraction. These minor differences do not appear to significantly impact the final radius size. The amplification of the group size, by a factor five as compared with its size before release, shows that dilution and dispersion act during the motion of the group down to the observation window.

The oriented eccentricity χ is also reported in figure 4(c) as a function of ξ. This figure points out the evolution of the anisotropy at large scales because of changes in the anisotropy of the elementary cylinders. Knowing χ and the radius R it is possible to calculate the semi-axis in the vertical and horizontal direction, which will be useful later. The average volume fractions of solid $\overline{\alpha}$ can be calculated using the relation $\overline{\alpha} = (\pi d/4w)\tilde{\alpha}$ from direct measurements of surface fraction $\tilde{\alpha}$. Then, a global volume fraction $\langle\overline{\alpha}\rangle$ can be obtained by averaging $\overline{\alpha}$ over the extension of the group. For runs involving groups of cylinders with the same injected mass $N_c\xi \approx 300$, its order of magnitude is

2 % and, for groups with $N_c\xi = 1000$, it is 3 %, being it intermediary for other cases. Note that this solid volume fraction averaged over the group can also be related to the measured size R by $\langle\overline{\alpha}\rangle = (N_c d^3\xi/4wR^2)$. This definition combined with the scaling law of R presented in figure 4 provides the estimation $\langle\overline{\alpha}\rangle = (\pi d/100w) \simeq 2.5$ % in agreement with the averaged value obtained from direct measurements.

These fairly diluted groups are expected to be in a regime similar to the well-known particle-settling regime usually observed far from the injection in unconfined clouds of particles at large Reynolds numbers (see Noh & Fernando 1993 or Kriaa *et al.* 2022 among others). In fact, two results clearly draw a comparison between the two cases: the cloud extension does not vary during its fall because the entrainment rate is very low, and the velocity of the group is of the order of magnitude of the terminal velocity (Kriaa *et al.* 2022). In our case, the reasons for rapidly reaching such a regime are simply that when the cloud radius R reaches the observed values, the mean distance between two cylinders estimated by $d_{12} = d\sqrt{\xi/\widetilde{\alpha}}$ becomes larger than the length of the cylinder $L = \mathrm{d}\xi$ and is at least of the order of the viscous length δ_ν. This length represents the length of attenuation of a velocity perturbation estimated as $\delta_\nu = V_\infty w^2/\nu/\kappa$ with $\kappa = 10$ (Filella, Ern & Roig 2015). As discussed in Noh & Fernando (1993), the group of cylinders thus interacts weakly and behaves as in particle-settling regimes. Due to confinement, turbulence cannot develop, and agitation induced in the liquid is characterised by length scales shorter than the group size. This favours this regime.

The following discussion shows that the flow presents an internal multi-scale organisation robust enough to build statistically reproducible internal heterogeneities.

4. Internal multi-scale spatio-temporal organisation

The mean velocity, shape and size of the groups have been discussed as global characteristics for cylinders and spheres. In addition, a detailed investigation of the internal spatio-temporal structure of the group can be conducted to discuss multi-scale organisation and its sensitivity to the primary anisotropy of the cylinders. Since the runs with spheres did not present multi-scale organisation, spheres being quite continuously distributed over the spatial extension of the groups, they will not be considered in this part.

4.1. *Solid phase heterogeneities at large length scale*

In figure 5 a representative cloud of cylinders is depicted in the reference frame of its centre of mass at different instants. Zoomed-in views are also provided to see in greater detail the internal organisation. In particular, it is observed that the spatial distribution of the cylinders in the group is heterogeneous, with areas of much greater extension than the length of a cylinder being devoid of cylinders, while others are highly concentrated. These large-scale regions evolve over time but quite slowly, allowing the spatio-temporal coherence of the overall movement of the group of cylinders to be followed with the naked eye. Another observation is that, at small scale, the cylinders form subgroups of cylinders in contact, rather than being entirely separated from one another. These subgroups or small-scale clusters are named objects in the following. Furthermore, the objects are constantly evolving in their configuration in reaction to the surrounding flow field. A statistical description of the objects is presented in § 4.3.

In order to visualise the heterogeneities of the group in a different way, figure 6(*a*) shows a view of the group, averaged over the time when the entire group of cylinders is fully visible in the window of observation. Being an average image created from binary ones, the observed greyscale levels correspond to the solid surface fraction. The red dashed line

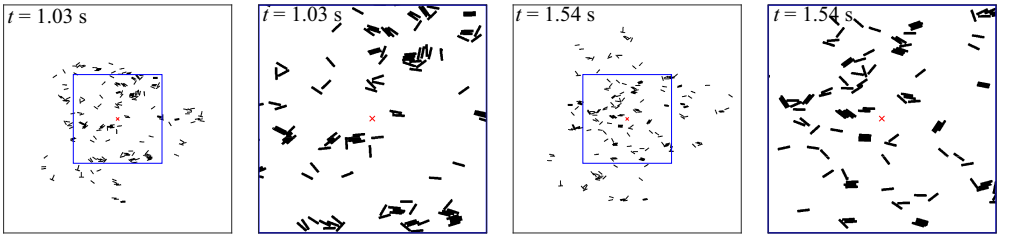

Figure 5. Images at two different instants of a group represented in the reference frame of its centre of mass, marked by the red cross ($\rho_c/\rho_f = 2.7$, $\xi = 5$, $N_c = 200$). From left to right: global view at instant $t = 1.03$ s, zoom on $t = 1.03$ s, global view at instant $t = 1.54$ s, zoom on $t = 1.54$ s. The global views show the whole group over a 20 cm extension; the blue rectangle designates the region of interest for the corresponding zooms.

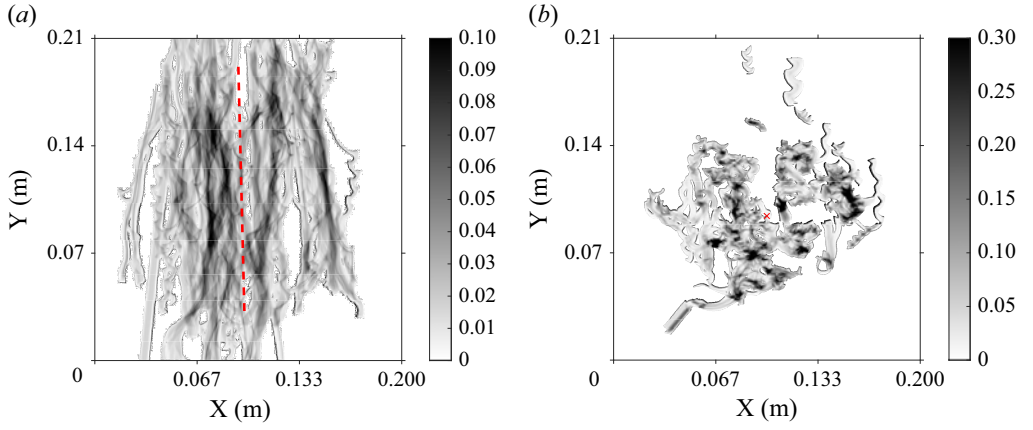

Figure 6. Image of the group obtained by averaging over time binary images ($\rho_c/\rho_f = 2.7$, $\xi = 5$, $N_c = 200$). (*a*) Average in a fixed window of observation when the whole group is inside. (*b*) Average in the reference frame of the group. In panel (*a*) (and (*b*) respectively), the red line (or red cross respectively) corresponds to the path (and position respectively) of the centre of mass of the group. The intensity of the grey levels are expressed as solid surface fractions.

indicates the path of the centre of mass. This figure is associated with a single release, and the lateral dispersion of paths that is visible is not representative of a statistically converged dispersion that remains negligible in this window of observation.

Significant disparities are observed, indicating that some paths are more frequently followed than others by many objects. Such over-concentrated areas are not the result of slower movements of objects that would lead to more frequent counting in the average. Preferential pathways are really present and are observed in movies of the fall of the group. These preferential pathways, referred to as 'streams', are observed in all the groups of falling cylinders that have been studied. The order of magnitude of their characteristic horizontal width is twice the length of a cylinder L in relation to the horizontal sizes of the objects they contain (see discussion in § 4.3.2). The measured solid surface fractions are naturally higher in the reference frame of the group (figure 6*b*). In this representation, strong heterogeneities at large scale in the distribution of cylinders are observed. They consist in over- or under-concentrated regions of varying extent. They are preferentially vertically oriented and may extend up to $2R$. Nevertheless, although many rearrangements occur, the group is observed over a relatively short period. Ultimately, over-concentrated large-scale structures exist within the group, which vary slowly and persist over significant

time scales and distances. These concentrated streams of cylinders appear similar to the vertical columnar structures observed by Huisman *et al.* (2016) in the experimental study of the sedimentation of inertial spherical particles, and by Fornari *et al.* (2018) or Moriche *et al.* (2023) in the numerical studies of the sedimentation of inertial oblate particles. Such elongated streams that propagate at large velocities were also observed to appear during the destabilisation of blobs of inertial particles by Zhao *et al.* (2014).

Whatever the cases, while the different releases show a considerable diversity in terms of group shape and spatial arrangement or heterogeneities at large scale, some similarities can also be noticed between them. Indeed, the solid fraction field shown for each group in figure 3 appears to be consistent, with a distribution that exhibits spatial variability but follows similar preferential vertically elongated patterns.

4.2. *Fluid phase heterogeneities at large length scale*

In figures 7(*a*) and 7(*b*) an instantaneous fluid velocity field associated with a group of cylinders in free fall is shown. Such velocity fields were obtained for one release using shadowgraphy-based particle image velocimetry (PIV) providing velocities integrated within the gap. During calculus, a mask was applied to prevent correlation with the cylinders' velocities. Figure 7 provides a fairly accurate representation of the type of flow generated and encountered by the cylinders. It clearly illustrates the high spatial heterogeneity of the fluid velocity field, particularly for the vertical velocities u_{fv} presented in the background of figure 7(*b*). Velocities are expressed in $\mathrm{m\,s^{-1}}$ in the laboratory frame of reference. The wakes of the objects are clearly visible, demonstrating that fluid is being drawn by each falling object. Additionally, due to the effect of flow bypass, the fluid rises on both sides of the objects and their wakes. This alternation of downward–upward flows at the individual object scale is replicated on the group scale, where a significant rise of the fluid on either side of the group is noted. Indeed, the spatial organisation of the background colour of figure 7(*a*) reveals a distribution of horizontal velocity u_{fh} characteristic of a global bypassing of the group by the surrounding fluid. Within the group, the velocity field is also far from uniform and shows this alternation at the scale of the streams with large upward currents. However, the upward vertical velocities are less intense than the downward vertical velocities and these upward velocities are more dispersed in space. Obviously, significant downward velocities appear to be correlated with areas of high cylinder concentration, which we previously referred to as streams or columnar structures as in Huisman *et al.* (2016). Furthermore, the absolute values of the downward velocities reach and even exceed those of the object velocities, in particular in the recirculating regions of the wake formed by objects or groups of objects.

In order to compare the velocity of the fluid to that of the solid phase, it is important to keep in mind that the presented results are built from measurements through a group of cylinders of finite size showing large and strong heterogeneities. The generic character of the measurements and their robustness concerning the spatial region where they are performed can thus be questioned. Figure 8 shows the probability density function (PDF) of the horizontal and vertical velocity fluctuations of the cylinders and of the liquid obtained from measurements in different zones, as represented on the left-hand side of the figure. A first noticeable result is that the PDF of the cylinders velocities is not sensitive to the five regions considered: all measured PDFs plotted in black superpose. These PDF will be discussed in § 5.2. On the contrary, the PDF of the fluid velocity fluctuations are sensitive to the region of measurement. Since flow perturbation around the group vanishes rapidly, the blue curves contain over-represented zero values. Even if they are not completely robust, the PDF provided by the polygon or by the circle of radius R regions are

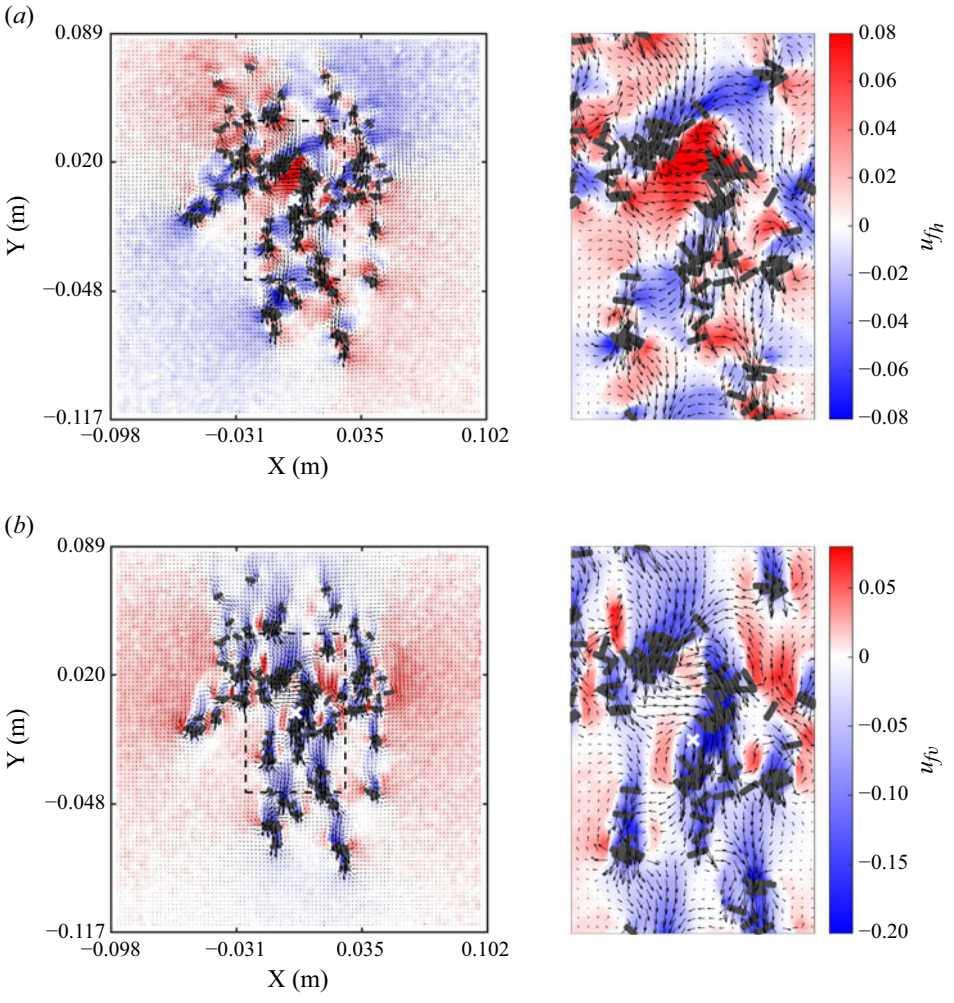

Figure 7. Instantaneous fluid velocity field obtained via shadowgraphy PIV in the laboratory reference frame ($\rho_c/\rho_f = 2.7, \xi = 5, N_c = 200$). The background colour indicates horizontal velocity in (*a*) and vertical velocity in (*b*). Left: full group visualisation; right: central group zoom. The white cross indicates the group's centre of mass and the dashed black rectangle highlights the zoomed area. Black arrows represent the velocity field, rectangles denote the cylinders. Velocity colour maps are expressed in m s^{-1}.

similar and can be considered as representative of the fluid velocity PDF inside the group and at its border. Orange and red curves are more representative of the liquid agitation in the core of the group, where higher velocity magnitudes occur. Whatever the region of observation, the PDF of horizontal velocities shows a smaller standard deviation for the liquid than for the cylinders. For the vertical velocity, it is also clear that, whatever the region of observation, the PDF are different for the liquid and the solid phases even if both show a dissymmetry indicating that cylinders and liquid are preferentially entrained downwards in the wakes of the objects present in the group. Very few cylinders are able to have upward velocities, whereas ascending liquid velocities are far more probable even in the core of the cloud of cylinders. They are the signature of large upward currents. As a consequence, the mean velocity of the liquid is far smaller than the mean velocity of the group of cylinders (see legend of figure 8). This result is in accordance with the general

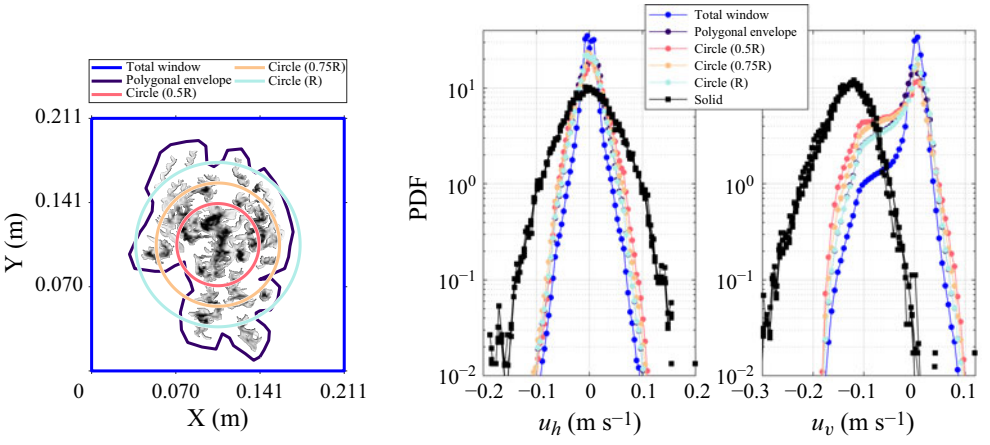

Figure 8. Robustness of the measurement of the probability density functions (PDFs) of the velocities of the cylinders and of the liquid (for $\rho_c/\rho_f = 2.7$, $\xi = 5$, $N_c = 200$). Five regions of measurement are considered: the entire observation window, the region inside the polygonal purple line delimiting the spatial distribution of $\overline{\alpha}$ or disks for which the radius is a given fraction (50 %, 75 % or 100 %) of R. Mean vertical velocity for the 50 % circle: -0.0356 m s^{-1}; for the 75 % circle: -0.0290 m s^{-1}; for the 100 % circle: -0.0181 m s^{-1}; for the polygon: -0.0205 m s^{-1}; for the blue window: -0.0050 m s^{-1}. The mean velocity of the solid is -0.125 m s^{-1}.

property of unconfined clouds in the particle-settling regime far from injection when the liquid no longer follows the particles. Here, the overall attenuation of the perturbations induced in the liquid due to confinement may impose such regime very rapidly after the injection.

4.3. *Spatio-temporal organisation at smaller scales*

In figure 5 it was observed that the clouds of cylinders are not a dispersal of cylinders dissociated from one another, colliding only intermittently. Instead, the clouds consist of subgroups of cylinders maintaining prolonged contacts, forming what are referred to as 'objects'. Any object is classified according to its number of cylinders in contact. With N denoting the number of cylinders involved, the object is said to belong to the class-N object. As shown in figure 7, objects are spread throughout the cloud. However, larger classes of objects seem to be preferentially associated with the large-scale streams already identified from the average surface solid fraction field (figure 6*b*). Being intermediary size groupings, they participate in building long vertical streams. These large streams reflect the tendency to form vertical clusters already observed in studies of particle suspension sedimentation in inertial regimes (see Uhlmann & Doychev 2014, Huisman *et al.* 2016, Fornari *et al.* 2018, Moriche *et al.* 2023). Here, due to the effect of confinement, the intermediary size groupings, which have a random life and a random organisation, are robust enough to be identified and analysed.

Throughout the series of conducted releases, a variety of contact arrangements between cylinders was observed, as illustrated in figure 9 for various classes. The different configurations are associated with relative movements between cylinders while maintaining contact. This occurs because the cylinders may reorient or slide over one another due to external forces exerted by the flow or due to direct contact between the cylinders. The relative motions of the cylinders inside an object, acting like a deformation, has not been characterised in the present study. We here focus our attention on its global

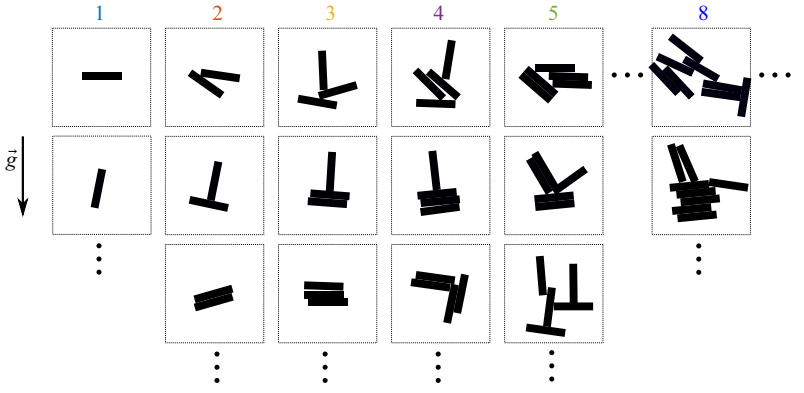

Figure 9. Non-exhaustive representation of the objects for different classes.

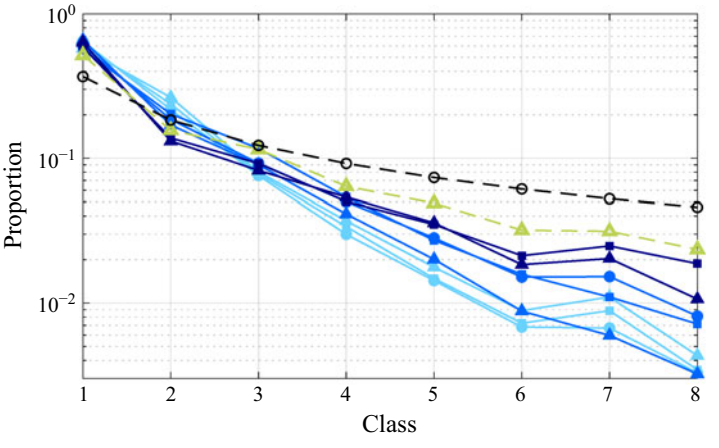

Figure 10. Proportion of the different classes within the different groups. Blue markers with solid lines: aluminium cylinders, $\rho_c/\rho_f = 2.7$; $\xi = 3$: ▲ $N_c = 100$, ■ $N_c = 200$, ● $N_c = 333$; $\xi = 5$: ▲ $N_c = 60$, ■ $N_c = 100$, ● $N_c = 200$; $\xi = 10$: ▲ $N_c = 50$, ■ $N_c = 100$. Green markers with dashed line: POMC cylinders, $\rho_c/\rho_f = 1.4$, $\xi = 5$: △ $N_c = 100$. The black dashed curve with empty circles shows a cylinders' uniform distribution between classes.

size, its lifespan (defined by the duration of sustained contacts between cylinders) and the way it interacts with other classes at its birth or death.

The developed PTV algorithm enables tracking of the centre of mass of the objects over time. Consequently, the velocities correspond to the barycentres of the objects and not those of the individual cylinders composing them. This tool makes it possible to address several questions regarding the internal behaviour of the groups. For example, what proportion of different classes exists within the group? Is one class more prevalent than another? What is the lifespan of these objects, and does it depend on their class? Additionally, what is the size of these objects, and how do they occupy space?

4.3.1. *Proportion of the different classes of objects*

To begin addressing these questions, figure 10 illustrates, for each experimental condition, the proportion of the different classes within the group, i.e. the number of objects in that class relative to the total number of objects. The black dashed curve represents the uniform distribution or equipartition, i.e. if the numbers of cylinders in each class were

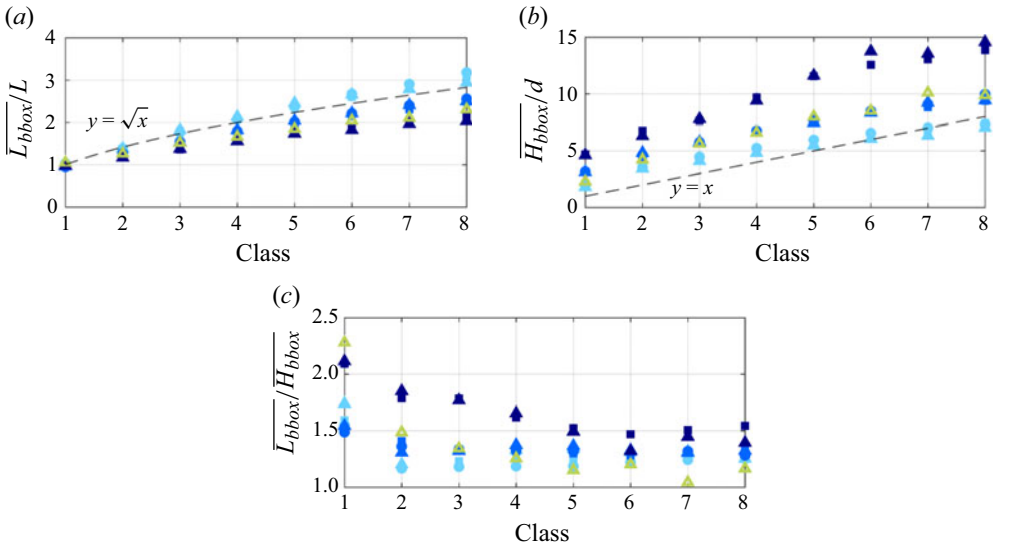

Figure 11. For all cases considered: (*a*) the average width of the bounding box, normalised with the length of a cylinder, the dashed line representing the curve $y = \sqrt{x}$; (*b*) the average height of the bounding box, normalised with the diameter of a cylinder, the dashed line representing the curve $y = x$; and (*c*) the ratio of the average width to the average height of the bounding box as a function of the object's class. Markers identical to those in figure 10 are used here and are detailed in table 1.

the same (n_1 cylinders in class 1, meaning there are n_1/N objects in class N). It can be observed that the greater the number of cylinders an object contains, the less likely it is to exist. Furthermore, classes 1 and 2 are over-represented (except for class 2 for groups with $\xi = 10$), whereas classes with $N > 3$ are significantly under-represented when compared with the uniform distribution between classes. These observations are general, regardless of the aspect ratio or the number of cylinders dropped, at least within the range of parameters studied. Remarkably, the number of objects in the different classes remains statistically stationary, while continuous reorganisations occur. Cylinders transition from one object of a class to another, but the overall proportion of the classes remains unchanged on average. For aluminium cylinders (blue curves), the aspect ratio has an effect on the proportion of the larger classes ($N > 5$). Specifically, longer aspect ratios tend to result in a higher proportion of larger classes. This could be related to an enhanced mechanical robustness of the large objects when ξ increases, whereas fluid disturbances that could destabilise these objects may be expected to have comparable kinetic energy in all cases, as they are created by solid displacements with mean velocities of the groups of the same order of magnitude. In fact, observation of the recordings reveals that the cylinders, due to the hydrodynamic torques acting on them, tend to orient themselves horizontally (perpendicular to the mean flow). Consequently, they tend to lie flat on top of one another. This configuration appears frequently, and is more robust when the cylinder is longer.

4.3.2. *Characteristic lengths of the objects of different classes*

A significant diversity in the shapes of objects within the group is observed. Although the internal orientation and arrangement of the various cylinders in the objects remain unknown, their bounding box sizes are available to us. This information can provide a more precise understanding of how these objects are organised, including their packing fraction, width, height and, consequently, how they are stacked. Figures 11(*a*) and 11(*b*)

respectively present, for all cases considered, the average width of the bounding boxes, $\overline{L_{bbox}}$, normalised with the cylinder length L and the average height of the bounding boxes, $\overline{H_{bbox}}$, normalised with the cylinder diameter d as functions of the object's class. The first noticeable observation is that the total number of cylinders N_c in each group does not determine the size of the objects, neither in the horizontal direction nor in the vertical one. Structuration of objects results from the hydrodynamic interactions to which they are submitted and from their own dynamic characteristics. In these experiments, the global solid fraction $\langle\overline{\alpha}\rangle$ and the velocity u_G do not vary significantly with N_c (§ 3). Thus, it is expected that the intensity of hydrodynamic interactions is not very sensitive to N_c. The structuration of objects of various classes is thus expected to be more sensitive to properties such as elongation ratio and density. In fact, a significant effect of the aspect ratio ξ and of the density ratio is visible in figure 11.

A clear variation in the average width and height of the bounding boxes is also observed depending on the class. While the number of cylinders increases by a factor of 8 from class 1 to class 8, the normalised bounding box width, $\overline{L_{bbox}}/L$, increases by a factor of 2 for the longest cylinders ($\xi = 10$), by a factor of 2.5 for cylinders with $\xi = 5$ and by a factor of 3 for the shortest ones ($\xi = 3$). The curve $y = \sqrt{x}$ allows us to compare $\overline{L_{bbox}}$ for a class-N object with the width $\sqrt{N}L$ of a reference object of the same class. When $\sqrt{N}$ is an integer, this reference object features $\sqrt{N}$ touching columns each containing $\sqrt{N}$ cylinders piled up horizontally. Such an object would have the height $\sqrt{N}d$ and an elongation ratio of ξ. It appears that, for aspect ratios other than $\xi = 3$, the average measured width of the objects is smaller than the width of this hypothetical object. Conversely, for $\xi = 3$, the objects of different classes appear a little wider than this reference object. It is concluded that, as the aspect ratio increases, the object's width decreases relative to that of the reference object, due to an enhanced possibility of vertical stacking.

The average measured height of the objects, normalised with the diameter d, is now considered and compared for each class N to a stack of height Nd (represented by the curve $y = x$). For all classes and all experiments (with the exception of $\xi = 3$, classes 7 and 8), the average height of the objects consistently exceeds that of a stack of cylinders oriented horizontally and piled up along the vertical direction. This outcome is expected, given that a wide range of random inclinations of the cylinders has been observed in the objects. It is also important to note that the average heights are smaller than the widths (figure 11*c*), and they do not exceed twice the length of a cylinder (figure 11*b*). This suggests that, nevertheless, the stacking predominantly occurs with moderate inclinations of cylinders. This observation is consistent with our scrutinising of the films, which reveals that when one cylinder is captured in the wake of another, it is drawn in through drafting and deposits itself onto the other cylinder, frequently horizontally. This stacking is stable, and less likely to be disturbed by cylinder interactions or hydrodynamic forces. Furthermore, hydrodynamic loads tend to reorient the cylinders perpendicularly to the flow, further promoting horizontal stacking. Since the cylinders' diameters are smaller than their lengths, these stacks are wider than they are tall. This phenomenon is a counterpart of the 'drafting, kissing, and tumbling' phenomenon described by Fortes, Joseph & Lundgren (1987) for spheres. In our case, the confinement of cylinders leads to a more stable post-contact arrangement, with the cylinders maintaining this configuration for a prolonged period before tumbling occurs at a later stage. This behaviour was similarly observed by Brosse & Ern (2011), in which the in-line fall of two disks in a three-dimensional tank and the role of the aspect ratio on the interaction behaviour was investigated. The numerical study by Moriche *et al.* (2023) examining the interaction of two oblate bodies also showed a strong effect of the anisotropy of the body, which remained in close proximity after

contact for a longer time than spheres. In the present study, it is observed that the larger the elongation ratio ξ, the larger the anisotropy shape ratio $\overline{L_{bbox}}/\overline{H_{bbox}}$, and that this ratio becomes independent of the class for classes greater than 3.

As opposed to the large-scale organisation of the whole group of released cylinders stretched in the vertical direction (§ 3.2), the anisotropy of the objects at small scale denotes the preferential horizontal orientation. This is completely consistent with both mechanisms creating the shapes: being it the preferential formation of vertical streams at large scale and being it the preferential piling of cylinders at small scale, both enhanced by increased ξ.

The compactness of the objects has also been measured. It is defined as the average of the ratio of the object's projected area occupied by its cylinders to the area of its bounding box, $A_{bbox} = \overline{L_{bbox}} \overline{H_{bbox}}$, which for a class-$N$ object, leads to a surface compactness equal to $NLd/\overline{A_{bbox}}$. This average compactness is not reported in a figure but there are several main ideas that can be noted. First, for all the cases and classes, the compactness does not depend significantly on the number of cylinders released (N_c). Also, the compactness of class 1 is different from that of all the other classes for which minor variations are observed from class to class. There is a sensitivity to the elongation ratio ξ, as the compactness decreases when ξ increases. For classes greater than 2, the compactness is equal to 0.37, 0.33, 0.26 and 0.35, respectively, for aluminium cylinders with $\xi = 3$, 5, 10 and plastic ones with $\xi = 5$. Such high compactnesses present in regions of a high concentration of cylinders activate descending motions of vertical streams. For class 1, the compactness values also decrease with increasing ξ, being of 0.5, 0.33, 0.22 and 0.38, respectively. The compactness measurement does not yield the value of one, as individual cylinders oscillate and reorient, causing their bounding box area to deviate from Ld.

4.3.3. *Focus on the second class of objects and on their preferential spatial arrangements*
So far, the proportion of the different classes, and their average characteristic lengths and compactness, have been reported. However, these provide only a global characterisation of the objects. It has also been observed that, although a wide range of arrangements is theoretically possible, all configurations are not equally observed. This result is investigated here for class 2. A refined algorithm was developed to accurately determine the orientation and the centres of mass of each cylinder within the object. It allows us to discuss the PDF of the angular difference $|\theta_2 - \theta_1|$, where θ_1 and θ_2 denote the orientations of the cylinders relative to the horizontal axis. These PDFs are plotted in figure 12 for three cases involving aluminium cylinders, with the same initial mass injected in each case, the only variable parameter being the aspect ratio ξ. Though all configurations exist, two are especially prevalent in class 2: the co-alignment of cylinders, where they are piled on top of each other with their axes of revolution collinear, and the inverted 'T' structures, particularly for shorter cylinders with $\xi = 3$ and 5. For $\xi = 10$, the co-aligned configuration remains predominant, while the inverted T structure is rarely observed. We attribute this difference to hydrodynamic effects that destabilise more efficiently inverted T structures when ξ increases. However, although the co-alignment configuration is predominant, the inverted T configuration, when it exists, exhibits a longer lifespan compared with co-alignment. For aspect ratios of $\xi = 3$ and 5, lifespans twice as long as those of the whole class 2 have been measured for the inverted T configurations, whereas co-aligned structures displayed lifespans similar to the whole class 2. This points out the noticeable robustness of inverted T structures for class-2 objects with $\xi \leq 5$.

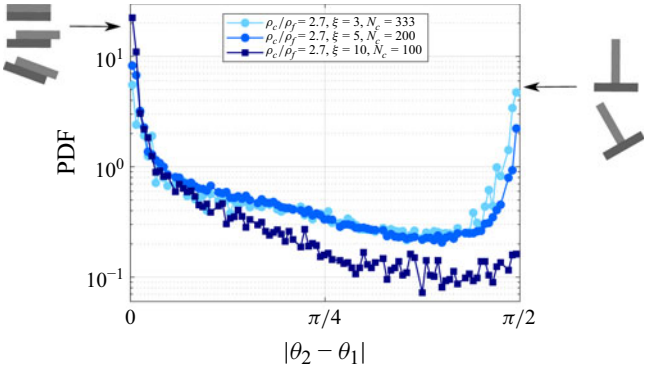

Figure 12. PDF of the angle formed between the two cylinders involved in objects of class 2 (unit is radian). For the three cases, the initial mass of injected cylinders is identical. The aspect ratio, and thus, the number of cylinders, differ between these cases. In grey, examples of possible arrangements between cylinders are shown for angular differences of $|\theta_2 - \theta_1| = 0$ and $\pi/2$.

4.3.4. *Lifespan of the different classes of objects*

In general, for all classes, it seems reasonable to assume that the confinement of the cylinders forces lasting interactions between them, as they cannot easily avoid one another being constrained to evolve within the cell plane, and that, consequently, the observed lifespans are longer compared with what can be expected in a three-dimensional tank. The average lifespans of the different classes are provided in figure 13(*a*) for all the cases and the PDFs of lifespans for each class are given in figure 13(*b*) for the case with $\rho_c/\rho_f = 2.7$, $\xi = 5$, $N_c = 200$.

Figure 13(*a*) illustrates how the normalised average lifespan of objects ($\bar{t}_{life}$) varies depending on the classes of objects. For the normalisation, the time $t_L = L/U_G$ required for the cloud to travel a distance equivalent to the cylinder length L is proposed. It should be noted that an object's life may end due to a range of factors, including contact with another object or fragmentation. The choice of t_L for normalisation will be justified in § 4.3.5 where reorganisation of the objects linked to the preferential loss or capture of a single cylinder will become evident. Figure 13(*a*) shows that, for all cases, the objects in class 1 generally exhibit a longer average lifespan compared with those in other classes. This corresponds to visual observations showing that single cylinders may more easily freely travel for long distances as compared with objects of a greater class. Indeed they can either snake in between large-scale vertical streams inside the whole group or they can bypass it going along the frontier of the dipolar structure it generates. Objects composed of a larger number of cylinders are observed to remain in contact for shorter durations, although from classes 4 to 8, average lifespans converge towards t_L except for the case with aluminium cylinders with $\xi = 3$ and $N_c = 100$. (Some data scattering due to less statistical convergence may also appear for class 8 or even for class 7.) This means that large classes travel a distance close to L during their lifespan. Coming back to the lifespan of class-1 objects, the figure 13(*a*) clearly shows that, for a given aspect ratio, the number of cylinders N_c within the group has a significant impact on it. The lifespan of class-1 objects decreases as the number of cylinders increases for a given aspect ratio and density ratio. This tendency is especially marked for aluminium with $\xi = 3$. For aluminium cylinders with $\xi = 5$ and $\xi = 10$, the same tendency is observed but t_L values are closer, and uncertainties do not allow for a definitive distinction between them. This decrease of $\bar{t}_{life}$ for the first class can be related to the fact that increasing the number of cylinders

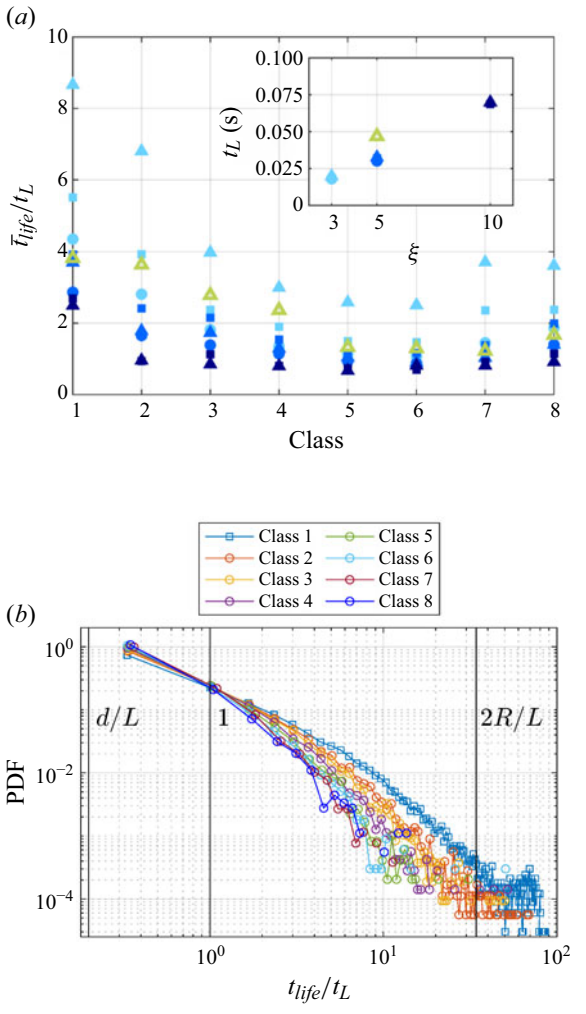

Figure 13. (*a*) Average normalised lifespan as a function of the object class. Lifespan is normalised with the time $t_L = L/U_G$ it takes for the cloud to travel a distance equivalent to the length of a cylinder L. This time t_L is provided in the inset figure. Markers are shown in figure 10 and listed in table 1. (*b*) Probability density function of the lifespan normalised by the time t_L for each class, for $\rho_c/\rho_f = 2.7$, $\xi = 5$, $N_c = 200$.

enhances the likelihood of interactions, thus reducing the lifespan of class 1. The inset of figure 13(*a*) indicates a linear evolution of t_L with ξ, as expected from the weak dependence of the mean fall velocity of the groups, U_G, on the aspect ratio (figure 2). The run with plastic cylinders at ξ =5 (plotted in green) has a time t_L greater than for aluminium cylinders, and the lifespans of classes 2–4 are higher for this case than for aluminium cylinders with the same N_c and ξ (plotted in intermediary blue). It was not possible to scale this density effect, but it originates from the differences of local solid-induced perturbations in the liquid strongly related to density for geometrically similar objects. Figure 13(*b*) presents the PDF of the normalised lifespan for different classes for the parameters $\rho_c/\rho_f = 2.7$, $\xi = 5$ and $N_c = 200$, the results provided being representative of the other parameter sets. Three characteristic values of $\bar{t}_{life}/t_L$ are reported in this figure: d/L, representing the dimensionless time required for the group to travel a distance equivalent to a cylinder diameter d, then the value 1, required to travel along the length

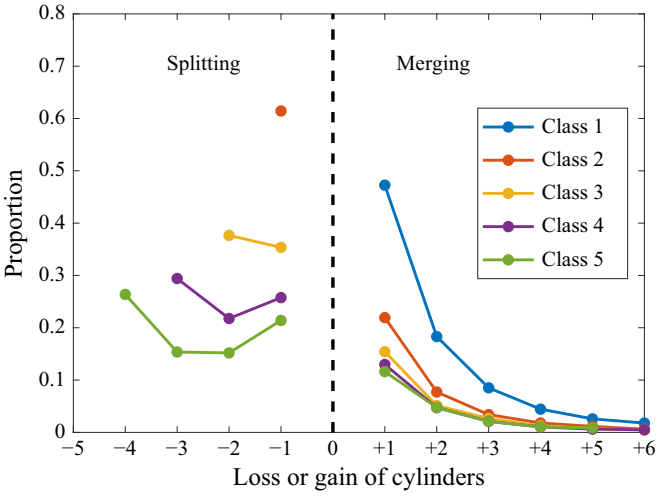

Figure 14. For the first five classes, the proportion of objects generated by losing (<0 values) or gaining (>0 values) cylinders for $\rho_c/\rho_f = 2.7$, $\xi = 3$ and $N_c = 333$. (Note that when an object of class N splits to form an object of class $N-1$, a class-1 object is also generated. So these two events should have equal probabilities. However, the measured probabilities differ slightly in our measurements. This is due to a difficulty in our algorithm in the analysis of deaths and births for a few special cases due to limited temporal resolution.)

of a cylinder L; and finally, $2R/L$, the dimensionless time required to travel along the group's diameter. The PDFs are decreasing when t_{life}/t_L increases for all classes, with shorter lifespans being the most probable. Very few objects persist beyond the time required to cross a group diameter. These properties indicate that the group and the objects it comprises are in constant evolution. Additionally, smaller classes are more likely to achieve longer lifespans, although from class 4 onwards, the PDFs become challenging to distinguish. The PDFs of all classes intersect at position $t_{life}/t_L = 1$. When the class increases, times t_{life} lower than t_L are more probable, while lifespans t_{life} greater than t_L are less probable. This is consistent with the preferential way of formation or ending life of an object through an interaction involving this object and a single cylinder, as discussed hereafter.

4.3.5. *Fate of objects after their 'death'*

In summary, the previous sections reveal that objects are more likely to consist of small classes, and that the most probable classes are also those with the longest average lifespans. This section examines how interactions between classes occur, focusing on the mechanisms driving their formation and destruction. Specifically, when an object of class N reaches the end of its life, whether by splitting or by merging, new objects appear that are named descendants. We examine here which classes the descendants belong to. Concerning splitting, the resulting classes are identified, while for merging, the class of the newly formed object is determined when contact occurs with another object. Figure 14 provides a detailed representation of this information for the first five classes of groups of cylinders with $\rho_c/\rho_f = 2.7$, $\xi = 3$ and $N_c = 333$. The interpretation of this specific case is representative of other cases with different injection conditions.

Each curve is associated with a given class (see the legend). Upon reaching the end of its life, an object of this class can either lose one or more cylinders, or merge with a single cylinder or an object composed of several cylinders. Similarly, objects are born through these breakups or coalescences. The x axis represents this loss or gain. For instance,

it has been observed that objects of class 2 (red curve) exhibit a strong tendency to either split into class-1 objects, losing one cylinder (-1), or to come into contact with a class-1 object to form a class-3 object ($+1$). Specifically, approximately 61 % loose one cylinder, while about 22 % gain a cylinder. More generally, for any class $N > 1$, the probabilities of generating descendants of classes $N + 1$ or $N - 1$ are the highest. These observations are crucial for understanding the formation and deformation processes of the objects. It is important to emphasise that class-1 objects, individual cylinders, are not only the most abundant within the group but also the most mobile. These objects frequently transition between classes, contributing to the formation and deformation of larger-class objects. From a hydrodynamic perspective, this behaviour can be interpreted as the flow being more likely to detach a single cylinder, the fundamental unit of a group, rather than breaking it into a dispersion of cylinders.

5. Statistical analysis of the kinematics

The preceding section offered a comprehensive analysis of the internal organisation within the group. Notably, the prominence of class 1 was emphasised, both in terms of its prevalence and extended lifespan, as well as its pivotal role in interactions between classes. However, the kinematics of objects within the group has not yet been addressed. In the present section, an in-depth discussion of the kinematics is presented.

Before analysing the statistics of the velocities of the cylinders present in the group, the meaning of the measurements obtained from the tracking algorithm must be clarified. First, individual cylinder velocities are not measured. The algorithm measures velocities of the centres of mass of the objects. Therefore, the internal kinematics and deformations of the objects remain unknown while the cylinders are in contact.

In this section a model for the mean vertical velocity of the group is first discussed (§ 5.1). Then, PDFs of the cylinder velocities are considered with a focus on how the motions are influenced by the cylinders orientations or by concentration effects. As agitation is influenced by the aspect ratio (ξ), the density ratio (ρ_c/ρ_f) and the number of injected cylinders (N_c), a normalisation of these PDFs is also proposed. In § 5.2 the statistics of the whole population of objects are discussed and in § 5.3 an analysis class by class is developed.

5.1. *Scaling law for the mean velocity of the group*

A model taking into account the main characteristics of the flow at large and local scales discussed previously is proposed to predict the mean fall velocity of the group of cylinders. The model takes into account dominant effects of heterogeneities at large scale, introduces their length dimensions and also the over-concentration measured at local scale for the largest class objects'. As the groups of spheres do not present such heterogeneities, the model cannot be applied to them. Considering also that the group of spheres moves with a mean velocity very close to the terminal velocity of the isolated sphere (§ 3.1), the idea of building a specific model for them was discarded.

To build a model for a group of objects, homogenisation appears as a powerful technique. The idea of the group considered as an isolated body has often been proposed, particularly for clouds of particles falling in the viscous regime. In such cases, the mixture of particles and fluid are treated as an equivalent fluid with effective density and viscosity (Hadamard 1911; Rybczynski 1911; Nitsche & Batchelor 1997). At large Reynolds numbers, Grace & Harrison (1967) also developed a model for two-dimensional bubbles evolving in fluidised beds – that is, for regions of void – similarly to Collins (1965). Figure 15 presents the average velocity field of objects within a cloud of confined

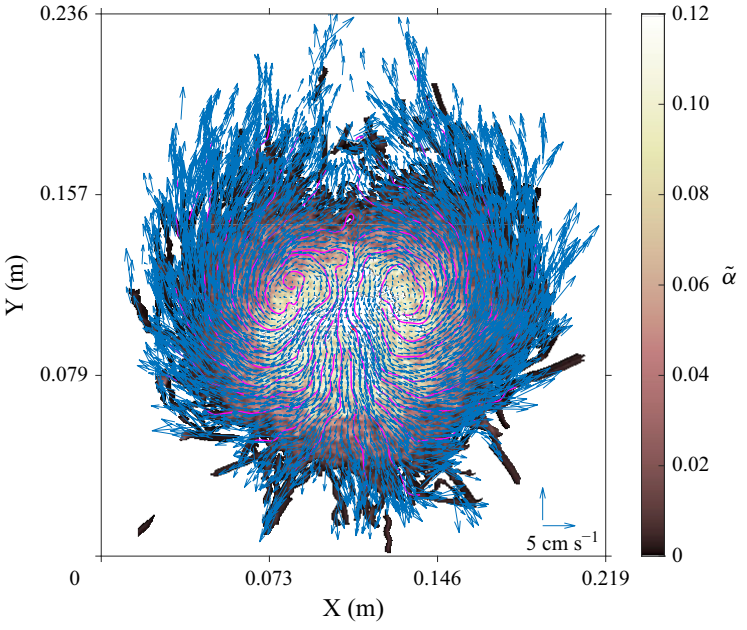

Figure 15. Averaged velocity field of the cylinders (blue vectors) and their path lines (magenta lines) overlaid on the surface fraction field of the solid (background) for which the colour map is provided. (Velocities are in the reference frame of the centre of mass of the group. Aluminium cylinders, $\xi = 3$, $N_c = 333$; 15 runs have been averaged.)

cylinders. Following the global motion of the group, the velocities are averaged over a great number of releases within an Eulerian grid with meshes of length L. The reported velocities are relative to the reference frame of the group's centre of mass. A dipolar structure emerges, accompanied by a downstream region where a few objects are evacuated from the dipole's wake. This dipolar structure appears when all the releases are averaged. It clearly reveals two characteristics of the groups valid whatever the release. First, it indicates that, for any release, in the reference frame of the laboratory, some cylinders go at lower velocity at the periphery of the group, being slowed down there by a reverse flow of liquid. Second, it shows how the motions of the cylinders are globally correlated by interstitial fluid motions and by their coupled spatio-temporal distribution. But this averaged vision of the group can be misleading. Indeed, for each release of a group of cylinders, a clearly heterogeneous organisation of the group falls through the confined cell consisting of large-scale vertical piles of cylinders around the centre of mass (see, for example, figure 7). So, this heterogeneity cannot be discarded in a model. Indeed, first attempts to model the motion of the group with an homogeneous approach lead to inaccurate predictions still dependent on ρ_c, N_C and ξ. Another argument that helps in understanding that a model with a homogeneous group cannot be applied is the large difference between the mean velocities of the fluid and of the cylinders inside the group (figure 6).

The main idea of the model we propose is to predict the velocity of the group as being that of the large-scale vertical piles of cylinders that are observed and that contain most of the cylinders. It is assumed that these piles behave like isolated equivalent bodies of horizontal dimension $\mathcal{A}$ and vertical dimension $\mathcal{B}$, with a density of the liquid–solid mixture occupying its volume $\rho_{eq} = (1 - \alpha_{sp})\rho_f + \alpha_{sp}\rho_c$, where α_{sp} is the solid volume fraction in the pile. This object is assumed to be submitted to its weight, Archimedes'

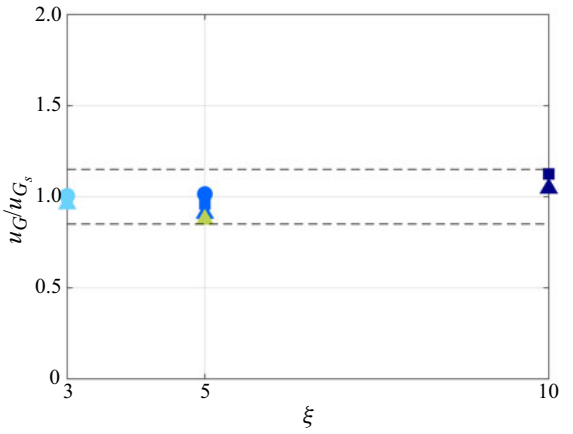

Figure 16. Mean vertical velocity u_G normalised with u_{G_s} as a function of the aspect ratio ξ. The dashed black curves represent a 15 % error margin.

buoyancy and an inertial drag due to the flow surrounding the pile of cylinders that also includes the effect of confinement in the cell. An inertial drag coefficient is introduced and denoted C_d. At equilibrium, this simplified momentum balance applied to the solid phase is written as

$$\frac{1}{2}\rho_f C_d u_{G_s}^2 \mathcal{A}w = (\rho_{eq} - \rho_f)\mathcal{A}\mathcal{B}wg, \tag{5.1}$$

where u_{G_s} is the predicted mean velocity of the pile assimilated to that of the group. The values of the lengths $\mathcal{A}$ or $\mathcal{B}$ are associated with the long vertical piles of objects present in the flow. Note that $\mathcal{A}$ disappears from the balance. The length $\mathcal{B}$ is taken proportional to the vertical semi-axis of the ellipses that represent the global group at large scale (§ 3.2). The length $\mathcal{B}$ is thus related to R and χ the radius and oriented eccentricity of the group and writes $\mathcal{B} = \beta_1\sqrt{\chi}R$, with β_1 a prefactor lower than 1 that should be common to all cases. Raw visual observation suggests that β_1 could be in the range $1/3 - 1/2$. In the present prediction, a value $\beta_1 = 1/2$ has been taken arbitrarily. On its side, the value of α_{sp} has to reproduce the over-concentration of cylinders in the piles. It has to be greater than $\langle\overline{\alpha}\rangle = \pi d/100w$. It is proposed to take α_{sp} proportional to the compactness of the bounding boxes of the objects of the larger classes (classes greater than 2, see § 4.3.2), denoted from now as α_{BB}. In fact, vertical streams of cylinders include many objects of large classes. The value of the solid volume fraction is written as $\alpha_{sp} = \beta_2(\pi/4)(d/w)\alpha_{BB}$ as α_{BB} is a surface fraction. It is important to choose $\beta_2 < 1$ to reproduce visual observations that show that the vertical alignments of heavy objects also present some unsteady empty zones such as wakes. The coefficient is fixed to a unique value, here also arbitrarily $\beta_2 = 1/3$.

This results in a group's mean velocity scale u_{G_s} that writes

$$u_{G_s} = \sqrt{\frac{2\alpha_{sp}}{C_d}\frac{(\rho_c - \rho_f)}{\rho_f}\mathcal{B}g} = \sqrt{\frac{\beta_1\beta_2}{C_d}\frac{\pi d}{2w}\alpha_{BB}\frac{(\rho_c - \rho_f)}{\rho_f}\sqrt{\chi}Rg}. \tag{5.2}$$

The drag coefficient and the global prefactor $\beta_1\beta_2/C_d$ are not known, but for the given values of β_1 and β_2, a unique value $C_D = 4.4$ can be chosen that best fits the data. Figure 16 shows the measured velocities normalised with u_{G_s}. Whatever the case, the ratio deviates from 1 by less than 15 %, indicating that the model provides an estimation at leading order of the fall velocities of the different groups considered by varying N_c, ξ or ρ_c.

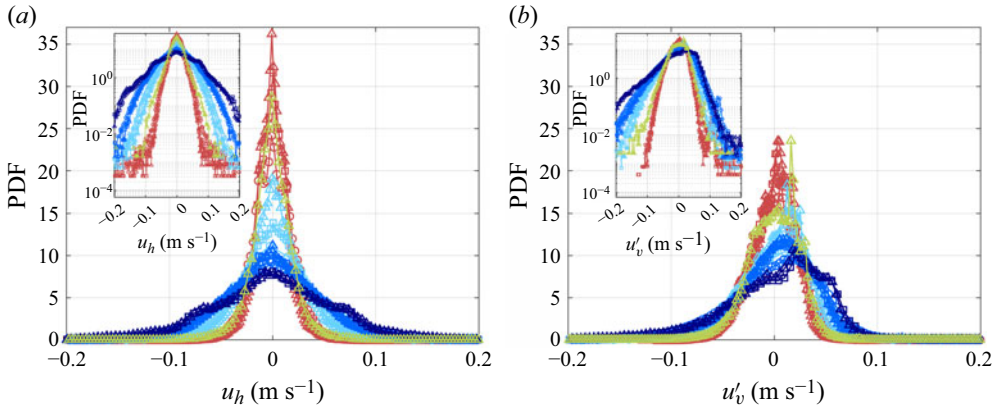

Figure 17. Overall PDF of the fluctuations of velocities of the objects present in the group. (*a*) The PDF of horizontal velocities and (*b*) the PDF of vertical velocities. Different cases: spheres in brown red; aluminium cylinders in blue – ξ increasing from light blue to intense blue – POMC cylinders in green (see all symbols in table 1).

5.2. *Probability density functions of the velocities for the whole population of objects*

Figure 17 presents the PDFs of the horizontal and vertical velocity fluctuations of the objects, $u'_v = u_v - u_G$ and $u'_h = u_h$, respectively. Note that the group velocity, u_G, is negative as the velocity is directed vertically downward. All PDFs of the horizontal velocities are symmetric whereas PDFs of the vertical velocities are asymmetric. The PDFs are less sensitive to N_c than to the elongation ratio ξ. Furthermore, the asymmetry of u'_v PDFs is enhanced when ξ increases.

The asymmetry of the PDFs of u'_v shows the tendency for most probable higher fall velocities. This may result from several mechanisms, such as interactions with fluid disturbances or direct interactions between objects, which could cause the objects – especially of class 1 or 2 – to tilt more and, consequently, increase their fall velocity. Another possible mechanism is the entrainment of objects in the wake of descending objects, particularly in streams that drag multiple objects along them. Both mechanisms are present in the flow and will be further discussed in §§ 5.2.1 and 5.2.2.

Focusing on aluminium cylinders and glass spheres that have similar densities, it is observed that groups with cylinders are more agitated than those with spheres, and that the higher the elongation ratio of the cylinders, the larger the standard deviation of the velocities, both horizontally and vertically. Also, for cylinders with the same elongation ratio $\xi = 5$, POMC objects are far less agitated than aluminium ones, which are associated with flatter PDFs of velocities. This behaviour can be related to the intrinsic dynamics of the cylinders, as when isolated, POMC cylinders show a rectilinear path in free fall while aluminium cylinders flutter. Similarly, for the most elongated aluminium cylinders ($\xi = 10$), in the PDF of u'_h two symmetric bumps are visible close to the standard deviation of the velocity for the periodic path of the isolated cylinder $\sqrt{u'^2_{h\infty}}/\sqrt{2}$ (see table 2). This also indicates, for $\xi = 10$, a stronger signature of the dynamics of single cylinders for objects present within the group.

The standard deviations of the horizontal and vertical velocities within the group, respectively $\sqrt{\overline{u'^2_h}}$ and $\sqrt{\overline{u'^2_v}}$, are now examined more precisely. They are plotted as a function of the aspect ratio ξ in figure 18. For aluminium material with $3 \leq \xi \leq 10$, increasing the elongation ratio of the elementary bodies leads to increased agitation,

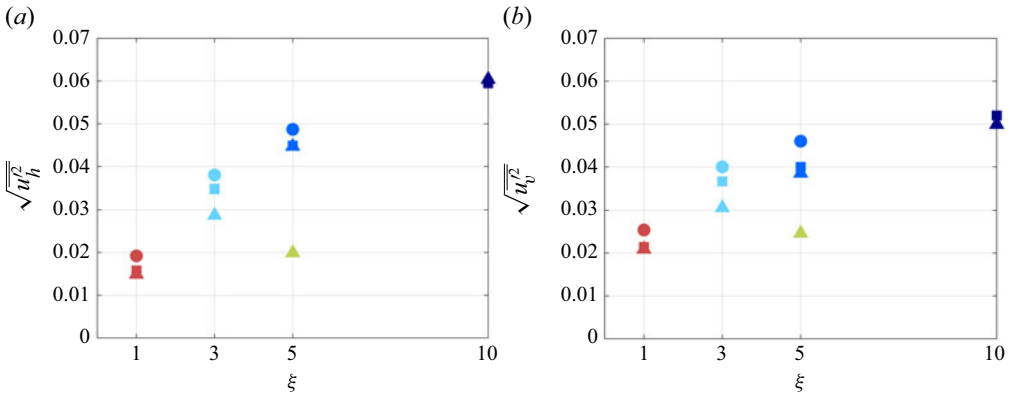

Figure 18. Standard deviations of velocities as a function of aspect ratio for the different cases: (*a*) horizontal velocities; (*b*) vertical velocities.

the effect being stronger on the horizontal component. In all cases, an increase in N_c also results in more significant agitation for a given aspect ratio, whatever the velocity component. But this enhancement is less and less important when ξ increases.

It is finally useful to compare the standard deviation of the horizontal velocity fluctuations in groups of aluminium cylinders to that of an isolated cylinder in free fall (see table 2). A primary observation emerges: for objects involving cylinders with $\xi \geq 5$, the horizontal agitation within the group corresponds nearly to that of the isolated cylinder. This suggests that horizontal agitation within the group is primarily attributable to the intrinsic dynamics of the cylinders associated with fluttering and vortex shedding. However, for objects made of cylinders with $\xi = 3$, the standard deviation in the horizontal direction is more or less 1.5 times greater than that of the isolated cylinder, denoting the impact on horizontal agitation of hydrodynamic interactions and a possible larger receptivity to hydrodynamical perturbations of objects involving shorter cylinders.

As previously observed in figure 17, the density ratio plays an important role in the agitation: given similar ξ =5 and N_c, objects resulting from groups of plastic cylinders show lower agitation than the aluminium ones for both velocity components. This is related to the fact that the present plastic cylinders do not oscillate when isolated. However, within the group, objects fall at velocities three times greater than the isolated cylinder, indicating that single cylinders or objects within the group are strongly responsive to wake entrainment by surrounding objects and to fluid agitation generated by wake interactions. The combined effects of the cylinder's proper dynamics and of the hydrodynamic interactions on the agitation of objects in any class within a cloud will be further discussed in §§ 5.2.3 and 5.3.

An important characteristic of the agitation concerns its anisotropy. The anisotropy factor of the objects' agitation within the group is defined as $\lambda_{v/h} = \sqrt{\overline{u_v'^2}}/\sqrt{\overline{u_h'^2}}$. For isolated cylinders in fluttering motion, in this range of elongation ratios, $\lambda_{v/h} < 1$. In the present experiments, for $\xi < 5$, we observe that $\lambda_{v/h} > 1$, even if $\lambda_{v/h}$ remains near unity. Plastic objects with $\xi = 5$ also present a larger group-induced agitation in the vertical direction. However, for ξ =10, the trend reverses for aluminium objects and $\lambda_{v/h}$ tends towards the value markedly lower than 1 found for isolated cylinders. It is noteworthy that in groups with the shortest ($\xi = 3$) and lightest cylinders, the agitation anisotropy is reversed compared with that of isolated cylinders. When immersed in group-induced fluid agitation, this reversal may be partially attributed to their lower weight, making them

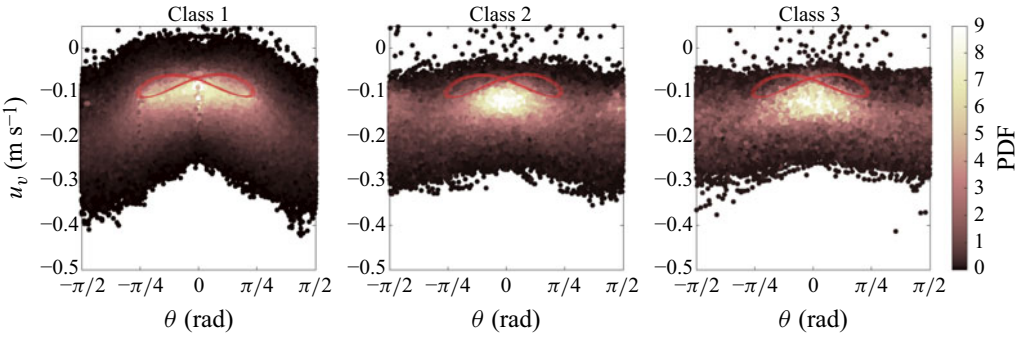

Figure 19. Vertical velocities of objects (from classes 1–3) as a function of their inclinations for groups with $\rho_c/\rho_f = 2.7$, $\xi = 5$ and $N_c = 200$. The colour map displays the bivariate PDF of these quantities. The red line corresponds to the behaviour of an isolated cylinder for comparison. (Horizontal orientation is an inclination equal to 0 rad.)

more responsive to fluid disturbances caused by the wakes of other cylinders and objects, potentially generating drafting effects. Additionally, the influence of regions of upward flow observed within the group contributes to the strong amplification of vertical agitation. This effect likely also influences horizontal agitation, by destabilising the body horizontal orientation that results in transverse displacements.

For spheres, the mechanisms governing agitation differ from those for cylinders. Specifically, the phenomenon initially described by Fortes *et al.* (1987), known as 'drafting, kissing, and tumbling', is observed, generating reorganisations between the spheres' relative positions and inducing both vertical and horizontal accelerations.

These initial observations of object velocities within the groups allowed us to quantitatively highlight differences between isolated cylinders and objects within groups. To disentangle the various effects (reorientation within the group or hydrodynamic interactions arising from collective behaviour), the following sections provide a detailed examination of the effects of reorientation and of local cylinder concentrations.

5.2.1. *Effect of the inclination of the objects on the vertical falling velocities*

The effect of inclination on the vertical velocities of objects is now examined (figure 19). Objects from the various classes, with the exception of class 1 (and also of class 2 for some aspects), exhibit similar behaviours (see § 5.3). Therefore, only classes 1, 2 and 3, being the most populated, have been represented. The red curves correspond to the relationship between velocity and inclination for an isolated cylinder. It should be recalled that the orientation of an object refers to that of the equivalent ellipsoid encompassing the entire object. In figure 19 the probability density within the phase space is represented by a colour scale. A clear correlation between vertical velocity and inclination is observed for class-1 objects. The highest falling velocities, even if not predominant, are achieved for inclinations of absolute values greater than $\pi/3$. The inverted 'V' shape of the distribution suggests a correlation between high velocity and significant inclination in class 1. However, it is also notable that the distribution is 'diffuse', different from that of the isolated cylinder, indicating that a range of velocities are experienced for a given inclination, and conversely, different inclinations correspond to the same velocity. The PDF indicates, however, that the most probable inclinations are close to those observed for the isolated cylinder. As observed for an isolated cylinder falling in liquid at rest, vertical inclination within the group is unstable, and cylinders that have been turned towards the vertical

experience a hydrodynamic torque that brings them back to the horizontal orientation. This explains the limited occurrence of the vertical positioning.

For classes other than class 1, the inverted V shape is less pronounced. Notably, high velocities are also observed for zero inclination, suggesting that, more than inclination, hydrodynamic interactions influence the velocity of the objects.

5.2.2. *Effect of solid concentration on the vertical velocities*

Even if the cylinders' orientation plays a significant role by generating high vertical velocities particularly for objects in class 1, for the other classes, high velocities are observed whatever their orientation. This implies the influence of additional mechanisms leading to agitation. Here, the correlation to local concentration within the cloud is examined, as visual observations revealed that concentrated areas exhibit faster descent velocities compared with the group as a whole. To define an instantaneous local concentration within a cloud, Voronoï tessellation is commonly used in point-particle swarms (Monchaux, Bourgoin & Cartellier 2010; Monchaux 2012). However, the large variable object sizes present here complicate tessellation without overlap. Therefore, a simplified method was used, involving averaged velocity and concentration fields. Since the local solid concentration changes slowly, it is measured as the average concentration over time, using an Eulerian approach in the reference frame of the centre of mass of the cloud as in figure 6(*b*). Given the strong spatio-temporal coherence of the concentration field, regions with high values of average concentration are strongly related to instantaneously concentrated areas. The concentration is a solid surface fraction $\tilde{\alpha}$, averaged over a grid with a mesh size equal to the length of a cylinder. Velocities were similarly averaged and the vertical component is denoted by $\tilde{u}_v$. We examine the correlation between these spatially and temporally filtered quantities, which vary randomly across the cloud and from run to run. In figure 20 the bivariate PDF of these variables is presented in colour scale. The horizontal dotted line represents the settling velocity of the group. Values above this line correspond to objects falling more slowly, while those below indicate faster descent. In regions of low concentration (e.g. $\tilde{\alpha} < 5\,\%$), predominantly slower velocities compared with the group are observed. This can be explained by the predominance of class-1 objects in regions between falling streams, which are more easily entrained by the upward fluid flows. However, in areas of low concentration, some objects also still exceed the group's mean velocity, potentially due to the ability of class-1 objects to adopt a vertical orientation. In highly concentrated regions (e.g. $\tilde{\alpha} > 15\,\%$), though less frequent, more probable velocities are descent velocities faster than the group, which can be attributed to objects positioned within the core of the streams, benefiting from the downward flow generated by the wakes of preceding objects.

5.2.3. *Towards a normalisation of the velocity PDFs*

In figure 21 the PDFs of the velocity fluctuations are normalised, whatever the cases, with their respective standard deviations. For each velocity component, they group on a single master curve, except for slight deviations observed on the tails. Fits of these PDFs averaged for all cases that use respectively symmetric and asymmetric generalised normal distributions are reported in Appendix A. To obtain a generic law for the velocity PDFs, scaling laws for the standard deviations based on the control parameters ξ, N_c and ρ_c/ρ_f have now to be found. As horizontal and vertical velocity fluctuations are considered on the basis of previous observations to be governed by different mechanisms, the scaling laws for their standard deviations will be discussed separately.

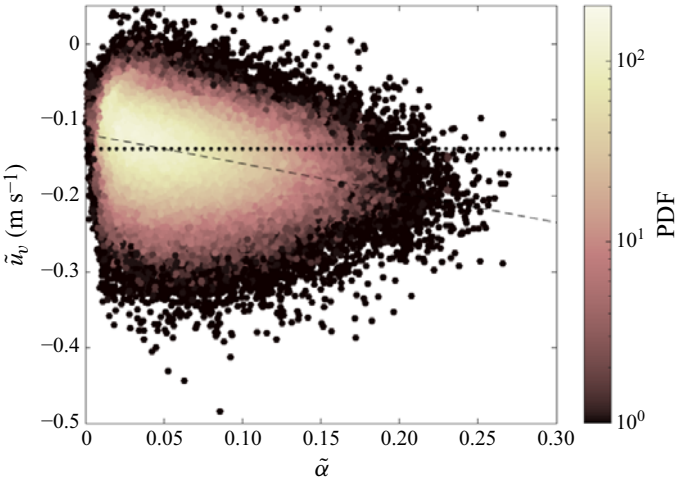

Figure 20. Locally averaged vertical velocities as a function of local solid surface fraction within groups with $\rho_c/\rho_f = 2.7$, $\xi = 5$ and $N_c = 200$. The colour scale represents the bivariate PDF of these variables. The dotted line marks the average fall velocity of the group. The thin dashed line is a linear regression of all points showing the overall trend.

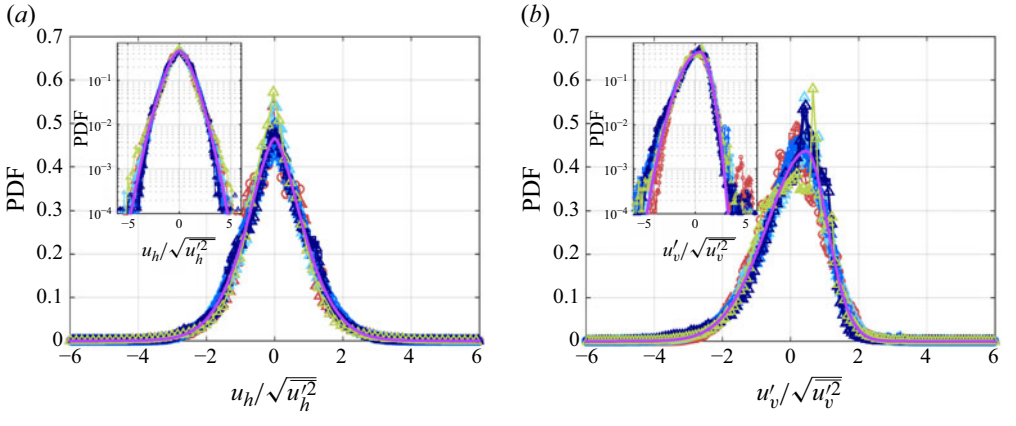

Figure 21. Overall PDF normalised with the standard deviation of objects' velocities for the different cases: (*a*) PDF of horizontal velocities; (*b*) PDF of vertical velocities. For both, an inset figure displays the same quantities on a semi-logarithmic scale. The purple curve is a fit for the average PDF across all cases (see Appendix A). Symbols are those of table 1.

5.3. *Scaling law for the standard deviation of the horizontal velocities.*

Group agitation is closely linked to the mobility of isolated cylinders. Specifically, class-1 objects, which are the most numerous, play a primary role in recombinations with other objects. This occurs through a peeling mechanism that laterally displaces cylinders towards the sides of larger-class objects. The scaling law for horizontal velocity is therefore assumed to involve a characteristic of the dynamics of an isolated cylinder. A relevant quantity that characterises the cylinder's dynamics is its natural frequency, rather than its average velocity or fluctuation amplitude in the isolated case. This frequency, f_θ, for which a scaling law has been established (Letessier *et al.* 2025), is reported in table 2.

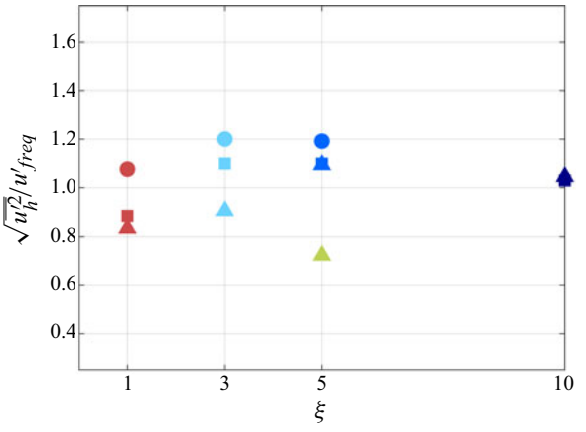

Figure 22. Normalisation of the standard deviation of horizontal velocities with u'_{freq} as a function of the aspect ratio, for the different cases investigated.

It characterises the cylinder's motion under permanent fluttering conditions. It reveals the intrinsic responsiveness of the cylinder to return to a horizontal position after being deflected by vortices generated in its wake. It is also the body's natural frequency, which manifests when, for example, the body in rectilinear flow is perturbed. Thus, this frequency is expected to be observable for plastic cylinders in a fluttering regime or during transients following perturbations. Moreover, this frequency remains unchanged even in the presence of an upward counter-current when cylinders are dropped in a stationary fluid (Letessier *et al.* 2025). In other words, it is an inherent property of the cylinder that may well be present within the group in the behaviour of objects. Using it, a velocity scale can be constructed by associating it with the cylinder's length scale L. This velocity is denoted u'_{freq}, and is defined as

$$u'_{freq} = L\frac{2}{T_\theta} = 2Lf_\theta, \quad \text{thus} \quad u'_{freq} = 2L \times 0.13\sqrt{\frac{(\rho_c - \rho_f)}{\rho_c}\frac{g}{L}} \tag{5.3}$$

following Letessier *et al.* (2025). The half-period of oscillation $T_\theta/2$ is chosen here, as the characteristic time required for a cylinder to complete a to-and-fro lateral excursion.

Figure 22 illustrates that normalisation with this velocity collapses the different aspect ratios and density ratios. Indeed, standard deviations of horizontal velocity differ by a factor of 3 between plastic and aluminium cylinders with $\xi = 5$, as well as between spheres and aluminium objects with $\xi = 10$, and when normalised, the discrepancies are now reduced to less than 30 %. It should be noted, however, that this frequency has not been identified for isolated spheres independently of this proposal. Also, the sensitivity of the standard deviations to N_c is not captured and is more important for lighter objects when hydrodynamics interactions also participate to the objects' dynamics.

5.4. *Scaling law for the standard deviation of the vertical velocities*

For the group of objects, in the vertical direction, the inherent dynamics of isolated cylinders is overtaken by vertical entrainment and shaking in wakes of neighbouring objects, and by motions induced by vertical streams. Those streams are primarily related to the elongation ratio ξ. A scaling law of the standard deviation in the form of a power law involving this dimensionless parameter, also with an assumed proportionality to the

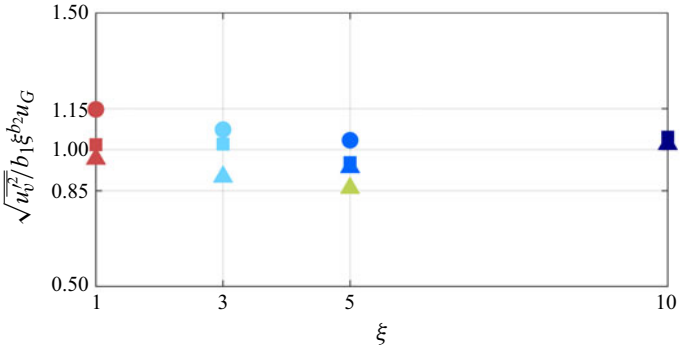

Figure 23. Normalised standard deviation of vertical velocities as a function of aspect ratio for $b_1 = 0.2$ and $b_2 = 0.4$.

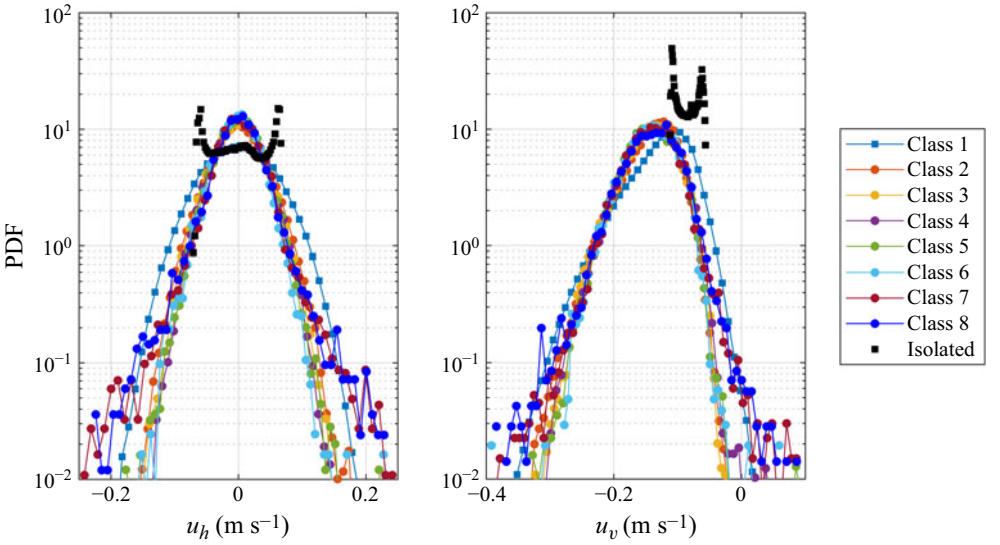

Figure 24. The PDF of the horizontal and vertical velocities of objects within the cloud for each class ($\rho_c/\rho_f = 2.7$, $\xi = 5$, $N_c = 200$). The black squares represent the PDF for an isolated cylinder.

group velocity u_G has been tested and proved to reproduce the physics: $\sqrt{\overline{u_v'^2}} = b_1\xi^{b_2}u_G$. By fitting this relation across all data sets for different initial release conditions, it is noted that a satisfying collapse is found. Figure 23 shows the normalisation where the coefficients were determined to be $b_1 = 0.2$ and $b_2 = 0.4$. Physical interpretation for this expression is however not obvious. It remains that it makes sense that on the one hand, ξ, and on another hand, u_G, which depends on large-scale dimensions and concentration of columnar streams (see relation 5.2), are both involved in this scaling law.

5.5. *Velocity statistics of the objects conditioned by class*

To provide a more refined analysis, the PDFs of object velocities can be examined separately for each class.

In figure 24 the distributions of horizontal and vertical velocities, u_h and u_v, are shown for the specific case: $\rho_c/\rho_f = 2.7$, $\xi = 5$, $N_c = 200$. Objects of class 1 exhibit PDFs of u_h

and u_v clearly distinct from those of the other classes. Moreover, velocity distributions of u_h, but also of u_v, superpose for all the classes different from the first one up to classes 7 and 8 for which larger tails appear. This property is observed for other values of ξ, ρ_c/ρ_f and N_c, even if in some cases the behaviour of class 2 also differs from the other ones as discussed hereafter.

The PDF of u_h for class 1 is more spread out, and this confirms a larger horizontal mobility compared with other classes. The horizontal velocity distribution for the isolated cylinder (drawn in black) is bimodal, a characteristic of oscillatory motion. In contrast, for all object classes in the group, zero horizontal velocity is most likely. For class 1 in the group, single cylinders being immersed in a field of fluid agitation, it can be understood that the PDF is no longer bimodal, as the introduction of noise into an oscillatory signal disrupts the bimodality of its PDF.

The asymmetric PDFs of vertical velocities, regardless of the object's class also show that the trace of the fluttering motion is lost. The objects within the group cover a wider velocity range, particularly at higher velocities, exceeding the velocity of the isolated cylinder by over four times for rare cases. Class 1 once again stands out, sometimes achieving lower velocities than the group and occasionally, though rarely, even ascending motions. Being the lightest class, it is most susceptible to counter-flows generated by the group. Higher classes can also experience a few upward velocities associated with combinations of large deformations and rotations.

Figure 25 presents the PDFs of horizontal and vertical velocities (figures 25*a* and 25*b,* respectively) for aluminium objects of classes 1 and 3, for three cases involving the same initial mass of injected cylinders but different aspect ratios. Class 3 is considered representative of the behaviour of all higher classes, as it only differs from higher classes in the extreme tails of the PDF. The black lines represent the velocity PDFs for an isolated cylinder. For both horizontal and vertical velocities, the distinction between class 1 and class 3 becomes far more pronounced as the aspect ratio increases. In the case of $\xi = 10$, the PDFs for class 1 (solid filled squares) exhibit a completely different shape from PDFs of higher classes, indicating that normalisation with the standard deviations would not be sufficient to collapse the curves. In fact, for this case, the PDFs of horizontal and vertical velocities of class 1 show a significant influence from the dynamics of an isolated cylinder, particularly within the velocity range corresponding to fluttering.

Finally, the mean fall velocity, the normalised standard deviations of both components of the velocity and the anisotropy ratio $\lambda_{v/h} = \sqrt{\overline{u_v'^2}}/\sqrt{\overline{u_h'^2}}$ are reported class by class in figure 26 for all the cases explored. The standard deviations are normalised with the values for isolated cylinders provided in table 2. The standard deviations for the case with POMC cylinders are not reported, as these cylinders do not oscillate when isolated. In figure 26(*d*), data for plastic cylinders are nevertheless included (in green).

It is visible that, in any case, an object of class 1 falls at a mean velocity lower than the other classes (and than u_G), which adopt quite the same mean fall velocity greater than u_G (figure 26*a*). For the reported cases, at given injection conditions, both velocity components also have standard deviations that become independent of the class rank more often for classes greater than 1, sometimes greater than 2 (figures 26*b* and 26*c*). Furthermore, class 1 exhibits consistently slightly greater agitation than the other classes. Two arguments may explain why classes greater than 2 or 3 exhibit the same agitation. Firstly, as shown in figure 13, the largest objects have similar lifespans and spend time deforming and transitioning between object classes. As a result, they exhibit comparable fluctuations due to a certain continuity in the contact events and lack of permanence in any class. Secondly, the width of these objects generally remains between 1 and 3 times

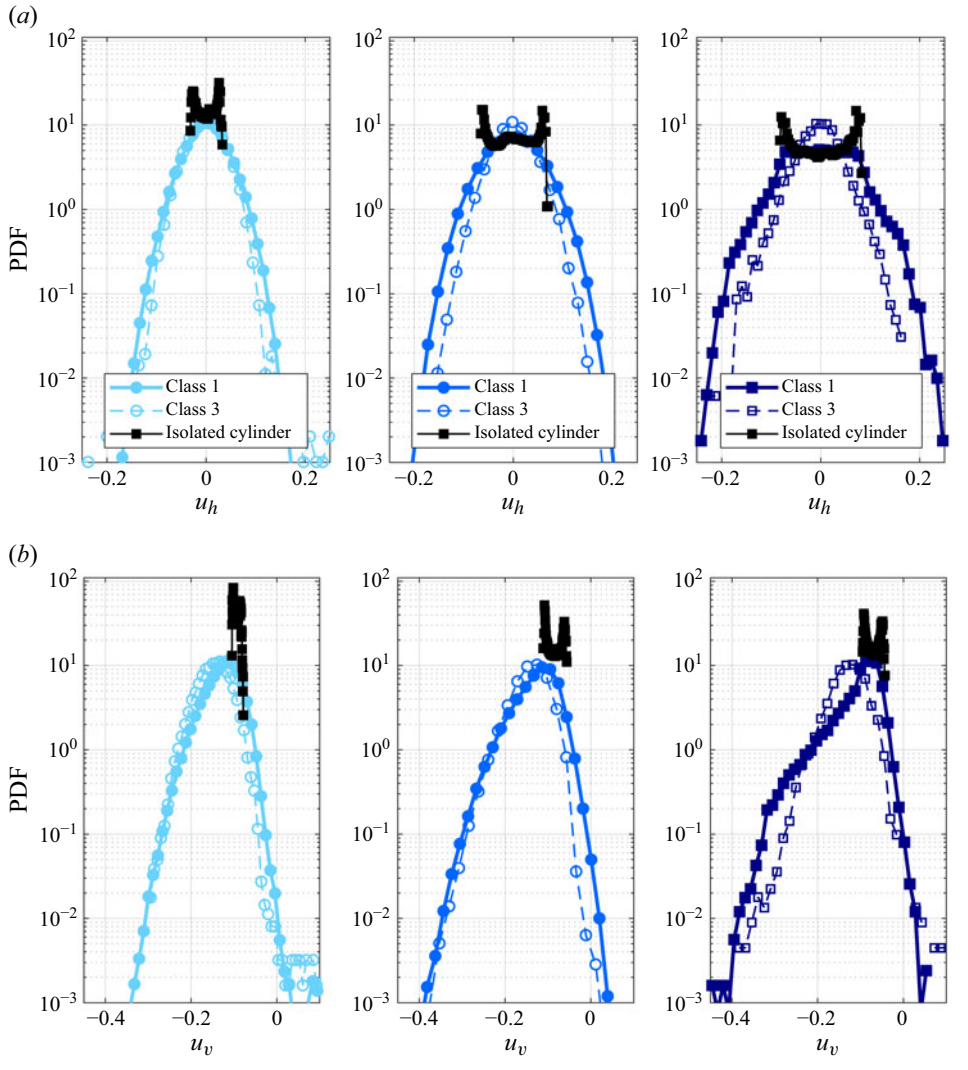

Figure 25. Probability density functions of the velocities of objects in class 1 and class 3 for three cases with the same initial mass of injected cylinders but different aspect ratios. From left to right, represented by colours ranging from light blue to dark blue: $\xi = 3$, $N_c = 333$; $\xi = 5$, $N_c = 200$; and $\xi = 10$, $N_c = 100$, all with $\rho_c/\rho_f = 2.7$. (*a*) Horizontal velocities; (*b*) vertical velocities. (Filled symbols: class 1; empty symbols: class 3; black symbols: isolated cylinder).

the cylinder length (see figure 11). Consequently, the wakes generated by all these objects, because they also fall at the same velocity, are similar, eliciting similar reactions from neighbouring objects.

For objects built with short aluminium cylinders ($\xi = 3$, plotted in light blue colour), whatever the velocity component, whatever their class, they exhibit increased agitation within the group as compared with $\sqrt{\overline{u_{h\infty}'^2}}$ or $\sqrt{\overline{u_{v\infty}'^2}}$ (figures 26*b* and 26*c*). Vertical agitation within the group may be more than quadrupled. Agitation is also enhanced when N_c increases, specially for the vertical component, as simultaneously, hydrodynamic interactions are stronger. These aluminium objects with $\xi = 3$ are preferentially reactive

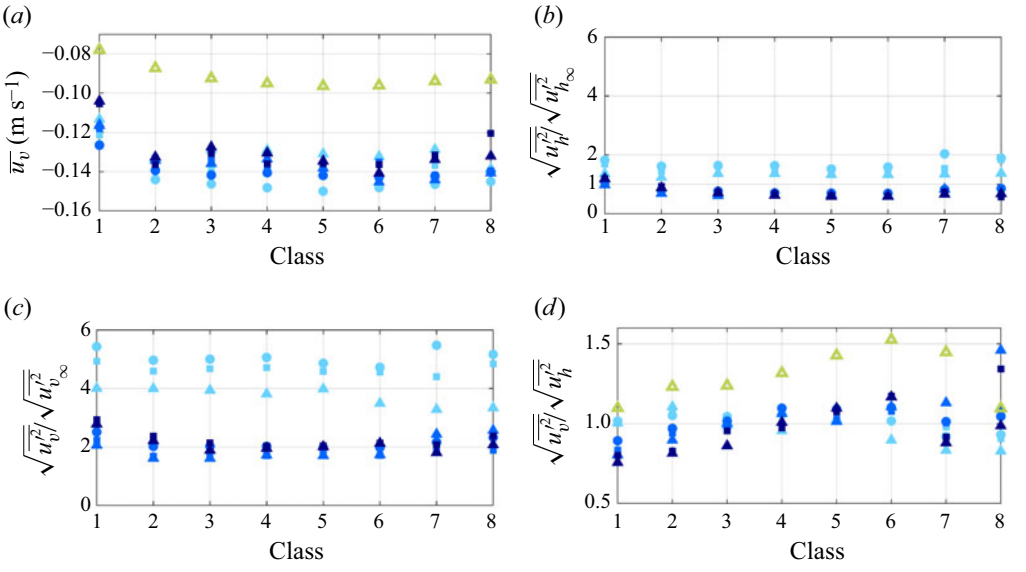

Figure 26. Evolution as a function of the class of: (*a*) mean velocity; (*b*) standard deviation of horizontal velocity, normalised with that of an isolated cylinder; (*c*) standard deviation of vertical velocity, normalised with that of an isolated cylinder; (*d*) anisotropy factor. The symbols used are identical to those detailed in table 1. Blue markers are used for aluminium cylinders with $\rho_c/\rho_f = 2.7$ and $\xi = 3$: ▲ $N_c = 100$, ■ $N_c = 200$, ● $N_c = 333$; $\xi = 5$: ▲ $N_c = 60$, ■ $N_c = 100$, ● $N_c = 200$; $\xi = 10$: ▲ $N_c = 50$, ■ $N_c = 100$. Green markers are used for POMC cylinders with $\rho_c/\rho_f = 1.4$ and $\xi = 5$: ▲ $N_c = 100$.

to fluid agitation generated by surrounding wakes and their agitation is nearly isotropic (figure 26*d*).

For all the cases with $\xi > 3$ (reported in more intense blue colours), the value of the standard deviation of the horizontal velocity for class 1 is equal to that of an isolated cylinder. Single cylinders in the group thus remain deeply marked by fluttering motions. For classes other than 1, a clear attenuation is visible for this horizontal agitation as compared with $\sqrt{\overline{u_{h\infty}'^2}}$. This is an important point, denoting that during their life these large objects are less easily shaken in the horizontal direction. Cases with $\xi = 5$ or $\xi = 10$ develop for the vertical velocity component a ratio $\sqrt{\overline{u_v'^2}}/\sqrt{\overline{u_{v\infty}'^2}}$ independent of N_c and of ξ. Its value is important, about 2, even if smaller than for the shorter cylinders. This underscores the substantial effects of hydrodynamic interactions along the vertical direction, due to wake-induced and columnar stream-induced fluid agitation.

The values of $\lambda_{v/h}$ for aluminium objects of class 1 decrease when ξ increases in the same manner as for the isolated cylinder. The aluminium objects with $\xi \geq 5$ present an anisotropy ratio that first increases when the rank of the class increases and then stabilises (excepted for class 8 for which data scattering does not allow us to conclude such findings). In these cases involving aluminium cylinders, $\lambda_{v/h}$ starts from a value lower than 1 for class 1. In classes 1 and 2, single cylinders and co-aligned cylinders are notably present (see figure 12), and react similarly to isolated cylinders, for which fluttering induced fluctuations are stronger in the horizontal direction. For greater classes, reference to the isolated cylinder is lost and the asymptotic value of $\lambda_{v/h}$ is around 1, denoting a convergence towards isotropy for the fluctuating motions of large classes.

Objects react with their own dynamics depending on their density and the responsiveness of the isolated cylinder they are built from. However, they are shaken by

fluid agitation resulting from interactions between the preferentially vertically induced perturbations of the wakes of surrounding objects and of the motions induced by columnar streams. The general behaviour of fluid agitation inside the group has not been explored. But, as shown for the case with aluminium cylinders at $\xi = 5$ and $N_c = 200$ in figure 8, an anisotropy of the fluid agitation can be expected. Indeed, for this case, standard deviations of the vertical and horizontal components of the fluid velocity, estimated in the circle of radius equal to 50 % of R, are respectively equal to 5.3 cm s^{-1} and 2.7 cm s^{-1}. As observed in unconfined flows for light oblates bodies (Fornari *et al.* 2018), it seems then meaningful that light POMC objects with $\xi = 5$ gain and produce a relatively large vertical agitation having a tendency to enhance, more than any other case, this preferential vertical response for larger classes (for which $\lambda_{v/h}$ tends towards 1.5). For class 8, the change is important, and it may be due to the enhanced ability of these objects to deformation and rotation.

6. Conclusion

The behaviour of a group of cylinders in free fall within a confined cell filled with quiescent water has been investigated, with particular emphasis on the influence of the cylinders' aspect ratio (ξ), the number of cylinders introduced (N_c) and the relative density (ρ_c/ρ_f). Spheres were also included for comparative purposes. Cylinders exhibiting contrasting sedimentation behaviours in quiescent fluids when isolated were considered: aluminium cylinders displaying oscillatory paths and plastic cylinders displaying rectilinear paths (Letessier *et al.* 2025). To ensure statistical convergence, an extensive series of release experiments was conducted. The results point out dynamical and structural features arising at both local and global scales.

After release from rest, the group evolves rapidly towards the slowly varying quasi-steady regime investigated here, featuring a constant mean fall velocity and a slowly varying characteristic size. Moreover, reorganisation phenomena continuously occur within the group. Observations revealed that the groups do not sediment as independent cylinders but form subgroups of cylinders in contact having variable lifespans. These subgroups, named objects, categorised into classes based on the number of constitutive cylinders, display diverse shapes and sizes. Generally, smaller objects are more numerous, with the relative distribution of classes within a cloud depending on the aspect ratio and density of the cylinders. However, this class distribution remains stable throughout the observation period, despite internal reorganisation of objects, suggesting a degree of dynamical coherence driven by hydrodynamic interactions and geometric arrangement.

The formation of objects strongly depends on the confinement, which prevents the cylinders from bypassing each other within the cell gap. Consequently, once a cylinder or an object is captured in the wake of another object, it is drawn into contact. Hydrodynamic couplings, including wake drafting and torque-induced horizontal alignment acting on single cylinders, stabilise the new object. The resulting contacts, predominantly along the axes, resist disruption by the flow more effectively than point contacts. However, flow agitation and shear act to destabilise these structures, while also facilitating their continual reformation. Despite these dynamic interactions, the overall group maintains consistent spatial extent and sedimentation velocity throughout the observation period.

Beyond individual objects, the clouds exhibit large-scale heterogeneities described as columnar 'streams' of densely packed aggregates aligned preferentially along the vertical. These streams, which generate significant local velocities, are separated horizontally by dilute regions allowing fluid to ascend relative to the cloud. These structures persist over time scales comparable to the observation period and extend over lengths comparable to the overall cloud size. They result from shape-induced piling, as observed in the

sedimentation of dilute suspensions of inertial oblate particles in quiescent fluids (Fornari, Picano & Brandt 2016; Moriche *et al.* 2023). This phenomenon underscores the interplay between local hydrodynamic clustering and global reorganisation of the flow field within the group.

Consistently across all parameter variations, the groups sediment at constant velocities, exceeding that of the isolated cylinders. For a given material and aspect ratio, the sedimentation velocity is at leading order unaffected by the number of cylinders, N_c. A model is proposed to reproduce the mean velocity of the group. It requires knowledge of, at large scale, the mean shape and size of the group and, at local scale, the compactness of the largest class objects. Indeed, the strong heterogeneity of the groups enforces motions of the objects deeply controlled by the vertical columnar streams, which need to be characterised at both scales.

For all the investigated cases, the PDFs of the velocity fluctuations of the objects constituting the group exhibit characteristic shapes that can be brought together in a generic curve when normalised with their standard deviation (at least for $\xi < 10$). Horizontal velocity PDFs are symmetric, while vertical velocity PDFs are asymmetric, reflecting preferential entrainment in object wakes and preferential vertical orientations of objects of classes 1 or 2. Two distinct mechanisms are identified as governing the velocity fluctuations: one for the horizontal component and another for the vertical one. The standard deviations of horizontal velocities are strongly linked to the intrinsic mobility of the cylinders that may give rise to specific translational and rotational motions characterised by an oscillation and vortex shedding frequency. However, the scaling proposed is not able to fully account for the influence of the particle number within the cloud. In contrast, vertical velocity fluctuations are primarily driven by the presence and interaction of objects' wakes and by the presence of solid concentrated regions that generate both descending and ascending flows, capable of accelerating or decelerating trailing objects. It is observed that fluctuation velocities of the objects within the group are influenced by concentration effects and by orientation of the objects. It was not possible, however, to disentangle both effects, even if it is clear that orientation is more efficient for lower classes. Specifically, the aspect ratio is identified as a dominant factor driving the fluctuations within the group and the fluid. This dependence is explained by variations with the aspect ratio in the columnar structure and in the relative distribution of object classes, which result in distinct fluctuations. A detailed analysis of the objects' agitation class by class showed that the signature of the proper dynamics of isolated cylinders is still present for class 1, and that the objects of the other classes display velocity fluctuations that do not depend on the class.

The results offer valuable insights into the intricate multi-scale dynamics governing the sedimentation of inertial anisotropic particles within confined geometries. They reveal the contrasted shape anisotropy that develops for clustering columnar structures and objects appearing at the various scales. Both are essentially due to, more or less stable, evolving packings, involving preferential piling of cylinders and entrainments in wakes.

As a final extension, we can consider how this flow would mimic the evolution of a group of cylindrical particles that would be released in an unconfined geometry. It can be expected that, in such a flow in which turbulent entrainment of fluid can develop, the release of a group of cylinders may first present a succession of regimes, as observed for spheres in Kriaa *et al.* (2022), before the particle-settling final regime, for which comparisons can be discussed, would be reached. In this final regime, it can be expected that the aspect ratio of the cylinders would play a large role in both large-scale and small-scale gatherings. Such considerations open attractive questions for future research.

Acknowledgements. We would like to thank S. Cazin, F. Bergame, H. Ayroles, E. Delsuc, R. Soeparno, S. Lun, L. Mouneix, G. Albert and M. Marchal for technical support.

Funding. We acknowledge financial support from ANR under the form of project 'Muscats' ANR-19-CE05–0010.

Declaration of interests. The authors report no conflict of interest.

Appendix A

The symmetric generalised normal distribution (Nadarajah 2005) can be written as

$$f_{sgnd}(x) = \frac{\beta}{2\alpha\Gamma(1/\beta)} e^{-\left(\frac{|x-\mu|}{\alpha}\right)^{\beta}}, \tag{A1}$$

where $\beta = 1.6$, $\alpha = 1.2$, $\mu = 0$ and $\Gamma(.)$ denotes the gamma function.

The asymmetric generalised normal distribution (Nacereddine & Goumeidane 2019) can be written as

$$f_{agnd}(x) = \begin{cases} \dfrac{\beta}{(\alpha_1+\alpha_2)\Gamma(1/\beta)} e^{-\left(\frac{-x+\mu}{\alpha_1}\right)^{\beta}} & \text{if } x < \mu, \\ \dfrac{\beta}{(\alpha_1+\alpha_2)\Gamma(1/\beta)} e^{-\left(\frac{x-\mu}{\alpha_2}\right)^{\beta}} & \text{if } x \geq \mu, \end{cases} \tag{A2}$$

where $\beta = 1.9$, $\alpha_1 = 1.7$, $\alpha_2 = 0.9$, $\mu = 0.5$ and $\Gamma(.)$ denotes the gamma function.

References

Bosse, T., Kleiser, L., Favre, J. & Meiburg, E. 2005*a* Settling and breakup of suspension drops. *Phys. Fluids* **17** (9), 091107.

Bosse, T., Kleiser, L., Härtel, C. & Meiburg, E. 2005*b* Numerical simulation of finite Reynolds number suspension drops settling under gravity. *Phys. Fluids* **17** (3), 037101.

Bouche, E., Roig, V., Risso, F. & Billet, A.-M. 2014 Homogeneous swarm of high-Reynolds-number bubbles rising within a thin gap. Part 2. Liquid dynamics. *J. Fluid Mech.* **758**, 508–521.

Bouchet, G. & Dušek, J. 2024 Path instabilities of freely falling oblong cylinders. *J. Fluid Mech.* **1000**, A54.

Brosse, N. & Ern, P. 2011 Paths of stable configurations resulting from the interaction of two disks falling in tandem. *J. Fluids Struct.* **27** (5–6), 817–823.

Buhler, J. & Papantoniou, D. 1991 *Swarms of coarse particles falling through a fluid*. Environmental Hydraulics.

Buhler, J. & Papantoniou, D.A. 2001 On the motion of suspension thermals and particle swarms. *J. Hydraul. Res.* **39** (6), 643–653.

Bush, J.W.M., Thurber, B.A. & Blanchette, F. 2003 Particle clouds in homogeneous and stratified environments. *J. Fluid Mech.* **489**, 29–54.

Collins, R. 1965 A simple model of the plane gas bubble in a finite liquid. *J. Fluid Mech.* **22** (4), 763–771.

Ekiel-Jezewska, M.L., Metzger, B. & Guazzelli, E. 2006 Spherical cloud of point particles falling in a viscous fluid. *Phys. Fluids* **18** (3), 038104.

Ern, P., Risso, F., Fabre, D. & Magnaudet, J. 2012 Wake-induced oscillatory paths of bodies freely rising or falling in fluids. *Annu. Rev. Fluid Mech.* **44** (2012), 97–121.

Faletra, M., Marshall, J.S., Yang, M. & Li, S. 2015 Particle segregation in falling polydisperse suspension droplets. *J. Fluid Mech.* **769**, 79–102.

Filella, A., Ern, P. & Roig, V. 2015 Oscillatory motion and wake of a bubble rising in a thin-gap cell. *J. Fluid Mech.* **778**, 60–88.

Fornari, W., Ardekani, M.N. & Brandt, L. 2018 Clustering and increased settling speed of oblate particles at finite Reynolds number. *J. Fluid Mech.* **848**, 696–721.

Fornari, W., Picano, F. & Brandt, L. 2016 Sedimentation of finite-size spheres in quiescent and turbulent environments. *J. Fluid Mech.* **788**, 640–669.

FORTES, A.F., JOSEPH, D.D. & LUNDGREN, T.S. 1987 Nonlinear mechanics of fluidization of beds of spherical particles. *J. Fluid Mech.* **177**, 467–483.
GIANORIO, L., D'ANGELO, M.V., CACHILE, M., HULIN, J.-P. & AURADOU, H. 2014 Influence of confinement on the oscillations of a free cylinder in a viscous flow. *Phys. Fluids* **26** (8), 084106.
GRACE, J.R. & HARRISON, D. 1967 The influence of bubble shape on the rising velocities of large bubbles. *Chem. Eng. Sci.* **22** (10), 1337–1347.
GUAZZELLI, É. & HINCH, J. 2011 Fluctuations and instability in sedimentation. *Annu. Rev. Fluid Mech.* **43** (1), 97–116.
HADAMARD, M.J. 1911 Mouvement permanent lent d'une sphere liquide et visqueuse dans un liquid visqueux. *C. R. Acad. Sci. Paris* **152**, 1735–1738.
HERZHAFT, B. & GUAZZELLI, E. 1999 Experimental study of the sedimentation of dilute and semi-dilute suspensions of fibres. *J. Fluid Mech.* **384**, 133–158.
HERZHAFT, B., GUAZZELLI, E., MACKAPLOW, M.B. & SHAQFEH, E.S.G. 1996 Experimental investigation of the sedimentation of a dilute fiber suspension. *Phys. Rev. Lett.* **77**, 290–293.
HU, J., YIN, Q., XIE, J., SU, X., ZHU, Z. & PAN, D. 2024 Settling dynamics and thresholds for breakup and separation of bi-disperse particle clouds. *Phys. Fluids* **36** (3), 033306.
HUISMAN, S.G., BAROIS, T., BOURGOIN, M., CHOUIPPE, A., DOYCHEV, T., HUCK, P., MORALES, C.E.B., UHLMANN, M. & VOLK, R. 2016 Columnar structure formation of a dilute suspension of settling spherical particles in a quiescent fluid. *Phys. Rev. Fluids* **1** (7), 074204.
KAJISHIMA, T. 2004 Influence of particle rotation on the interaction between particle clusters and particle-induced turbulence. *Intl J. Heat Fluid Flow* **25** (5), 721–728.
KRIAA, Q., SUBRA, E., FAVIER, B. & LE BARS, M. 2022 Effects of particle size and background rotation on the settling of particle clouds. *Phys. Rev. Fluids* **7** (12), 124–302.
LAI, A.C.H., WANG, R.-Q., LAW, A.W.K. & ADAMS, EE. 2016 Modeling and experiments of polydisperse particle clouds. *Environ Fluid Mech.* **16**, 875–898.
LAI, A.C.H., ZHAO, B., LAW, A.W.K. & ADAMS, EE. 2013 Two-phase modeling of sediment clouds. *Environ Fluid Mech.* **13**, 435–463.
LEE, A.T., RAMOS, E. & SWINNEY, H.L. 2007 Sedimenting sphere in a variable-gap Hele–Shaw cell. *J. Fluid Mech.* **586**, 449–464.
LETESSIER, D., ROIG, V. & ERN, P. 2025 Fluttering motion of a confined cylinder falling freely in fluid at rest. *J. Fluid Mech.* **1002**, A46.
MACHU, G., MEILE, W., NITSCHE, L.C. & SCHAFLINGER, U. 2001 Coalescence, torus formation and breakup of sedimenting drops: experiments and computer simulations. *J. Fluid Mech.* **447**, 299–336.
MACKAPLOW, M.B. & SHAQFEH, E.S.G. 1998 A numerical study of the sedimentation of fibre suspensions. *J. Fluid Mech.* **376**, 149–182.
METZGER, B., BUTLER, J.E. & GUAZZELLI, E. 2007*a* Experimental investigation of the instability of a sedimenting suspension of fibres. *J. Fluid Mech.* **575**, 307–332.
METZGER, B., GUAZZELLI, E. & BUTLER, J.E. 2005 Large-scale streamers in the sedimentation of a dilute fiber suspension. *Phys. Rev. Lett.* **95**, 164506.
METZGER, B., NICOLAS, M. & GUAZZELLI, E. 2007*b* Falling clouds of particles in viscous fluids. *J. Fluid Mech.* **580**, 283–301.
MOGHADARIPOUR, M., AZIMI, A.H. & ELYASI, S. 2017 Experimental study of oblique particle clouds in water. *Intl J. Multiphase Flow* **91**, 101–119.
MONCHAUX, R. 2012 Measuring concentration with Voronoï diagrams: the study of possible biases. *New J. Phys.* **14** (9), 095013.
MONCHAUX, R., BOURGOIN, M. & CARTELLIER, A. 2010 Preferential concentration of heavy particles: a Voronoï analysis. *Phys. Fluids* **22** (10), 103304.
MORICHE, M., HETTMANN, D., GARCIA-VILLALBA, M. & UHLMANN, M. 2023 On the clustering of low-aspect-ratio oblate spheroids settling in ambient fluid. *J. Fluid Mech.* **963**, A1.
MORTON, B.R., TAYLOR, G.I. & TURNER, J.S. 1956 Turbulent gravitational convection from maintained and instantaneous sources. *Proc. R. Soc. Lond. A Math. Phys. Sci.* **234**,1196, 1–23.
NACEREDDINE, N. & GOUMEIDANE, A.B. 2019 Asymmetric generalized Gaussian distribution parameters estimation based on maximum likelihood, moments and entropy. In *2019 IEEE 15th International Conference on Intelligent Computer Communication and Processing (ICCP)*, pp. 343–350. IEEE.
NADARAJAH, S. 2005 A generalized normal distribution. *J. Appl. Stat.* **32** (7), 685–694.
NITSCHE, J.M. & BATCHELOR, G.K. 1997 Break-up of a falling drop containing dispersed particles. *J. Fluid Mech.* **340**, 161–175.
NOH, Y. & FERNANDO, H.J.S. 1993 The transition in the sedimentation pattern of a particle cloud. *Phys. Fluids A: Fluid Dyn.* **5** (12), 3049–3055.

PARK, J., METZGER, B., GUAZZELLI, E. & BUTLER, J.E. 2010 A cloud of rigid fibres sedimenting in a viscous fluid. *J. Fluid Mech.* **648**, 351–362.

PAVLOV, L., CAZIN, S., ERN, P. & ROIG, V. 2021 Exploration by shake-the-box technique of the 3D perturbation induced by a bubble rising in a thin-gap cell. *Exp. Fluids* **62**, 22.

PIGNATEL, F., NICOLAS, M. & GUAZZELLI, E. 2011 A falling cloud of particles at a small but finite Reynolds number. *J. Fluid Mech.* **671**, 34–51.

RYBCZYNSKI, W. 1911 Uber die fortschreitende bewegung einer flussigen kugel in einem zahen medium. *Bull. Acad. Sci. Cracovie A* **1**, 40–46.

SEMIN, B., DECOENE, A., HULIN, J.-P., FRANÇOIS, M.L.M. & AURADOU, H. 2012 New oscillatory instability of a confined cylinder in a flow below the vortex shedding threshold. *J. Fluid Mech.* **690**, 345–365.

SEYED-AHMADI, A. & WACHS, A. 2021 Sedimentation of inertial monodisperse suspensions of cubes and spheres. *Phys. Rev. Fluids* **6** (4), 044306.

SUBRAMANIAN, G. & KOCH, D.L. 2008 Evolution of clusters of sedimenting low-Reynolds-number particles with Oseen interactions. *J. Fluid Mech.* **603**, 63–100.

TOUPOINT, C., ERN, P. & ROIG, V. 2019 Kinematics and wake of freely falling cylinders at moderate Reynolds numbers. *J. Fluid Mech.* **866**, 82–111.

UHLMANN, M. & DOYCHEV, T. 2014 Sedimentation of a dilute suspension of rigid spheres at intermediate Galileo numbers: the effect of clustering upon the particle motion. *J. Fluid Mech.* **752**, 310–348.

UHLMANN, M. & DUŠEK, J. 2014 The motion of a single heavy sphere in ambient fluid: a benchmark for interface-resolved particulate flow simulations with significant relative velocities. *Intl J. Multiphase Flow* **59**, 221–243.

VOTH, G.A. & SOLDATI, A. 2017 Anisotropic particles in turbulence. *Annu. Rev. Fluid Mech.* **49** (2017), 249–276.

ZAIDI, A.A., TSUJI, T. & TANAKA, T. 2014 Direct numerical simulation of finite sized particles settling for high Reynolds number and dilute suspension. *Intl J. Heat Fluid Flow* **50**, 330–341.

ZHAO, B., LAW, A.W.K., ADAMS, E.E. & ER, J.W. 2014 Formation of particle clouds. *J. Fluid Mech.* **746**, 193–213.